



Passive Beam Field Characterization for Application in Radiobiology

María del Hénar Rituerto Prieto

Passive Beam Field Characterization for Application in Radiobiology

by

María del Hénar Rituerto Prieto

to obtain the degree of Master of Science in Biomedical Engineering
at the Delft University of Technology,
to be defended publicly on Tuesday September 29, 2020 at 14:00 PM.

Student number: 4917812
Project duration: December 2, 2019 – September 29, 2020
Committee: Dr. Ir. Danny Lathouwers (Chair) TU Delft
Dr. Zoltán Perkó TU Delft
Dr. Erik van der Kolk TU Delft
Dr. Marta Rovituso HollandPTC

Contents

Abstract	v
Preface	vii
Introduction	ix
1 Theoretical Background	1
1.1 Physical Aspects of Radiotherapy with Proton Beams	1
1.1.1 Energy deposition in matter: Bethe-Bloch formulation	1
1.1.2 Lateral beam spread: Multiple Coulomb Scattering	2
1.1.3 Nuclear interactions	3
1.2 Biology of Therapeutic Proton Beams	4
1.3 Basis of Beamline Design	4
1.3.1 Passive scattering technique	5
1.4 Basis of Monte Carlo Simulations	7
1.4.1 Monte Carlo particle tracking and handling of secondary particles	7
1.4.2 Proton physics definition in Monte Carlo methods	8
1.4.3 Monte Carlo codes	8
1.5 TOPAS	8
2 Literature Study	11
2.1 Approaches to Build a Monte Carlo Simulation for Passive Scattering Systems	11
2.1.1 Nozzle simulation accuracy	11
2.1.2 Characterizing the beam entering the treatment head	12
2.2 Benchmarking Monte Carlo models using experimental data	13
2.2.1 Pristine Bragg peaks and SOBPs	14
2.2.2 Lateral profiles	16
2.3 Literature Study Conclusions	18
3 Materials and Methods	19
3.1 The HollandPTC Proton Therapy Center	19
3.2 Experimental Setup	20
3.2.1 The passive scattering system at HPTC bunker	20
3.2.2 Detectors	21
3.2.3 Passive Field Characterization	22
3.3 TOPAS Simulations	24
3.3.1 Simulation settings	24
3.3.2 Data analysis and statistical uncertainty	25
3.3.3 Validation of the pencil beam	25
3.3.4 Passive scattering simulations	26
4 Results and Discussion	29
4.1 Validation of the Pencil Beam	29
4.2 Passive Scattering Fields	35
4.3 Comparison of Experimental Data vs TOPAS Simulations for the Passive Scattering Setup	39
5 Conclusions and Future Prospects	49
Bibliography	53

Abstract

The main challenge of radiotherapy, used for treating cancer, is to deposit the prescribed dose in the tumor volume while sparing the surrounding tissue. The depth-dose distribution of protons makes proton therapy an alternative to conventional radiotherapy for some tumor sites. Having a better knowledge of the proton radiobiological mechanisms can potentially improve the effectiveness of radiotherapy treatments.

Holland Proton Therapy Center (HPTC) is one of the three Dutch proton therapy center. One of the purposes of its dedicated experimental beamline is to perform radiobiological experiments. In order to conduct all the different types of pre-clinical experiments, the beamline has to be equipped to provide large field irradiation with precise dose characterization. Moreover, having a reliable Monte Carlo (MC) model of the system allows to perform *in silico* verification of the beamline design and contribute to its optimization. In this context, the two main goals of this master thesis project were: to implement a dual ring scattering system in the experimental room of HPTC to produce homogeneous fields of different sizes; to create a MC model of the HPTC passive scattering beamline able to reproduce the experimental setup.

A dual-ring double scattering system was implemented in the HPTC horizontal beamline, starting from a single pencil beam at 150 MeV. The resulting passive irradiation fields were characterized by measuring and analyzing the lateral beam profiles, the depth-dose distributions and the relative dose at target position. Moreover, the beam characteristics and the setup were implemented in the TOPAS MC code. The beam source parameters, used as input of the MC model, were found by comparing the experimental and simulated beam envelope and depth-dose distributions of the pencil beam. Then, the complete scattering system model was benchmarked with experimental data by evaluating the lateral profiles, Bragg curves and dose distributions.

The results show that the implemented double passive scattering system can achieve dose uniformity between 96% and 99% for field sizes between $4 \times 4 \text{ cm}^2$ and $20 \times 20 \text{ cm}^2$ for a 150 MeV proton beam. Moreover, using a collimator with a $5 \times 5 \text{ cm}^2$ aperture, uniformity of at least 97% in the different Bragg peak regions is achieved. A good uniformity is also obtained for beam energies in the range 115 MeV-150 MeV, showing the robustness of the setup. Furthermore, the range of the proton beams passing through the beam-shaping elements, as well as the energy arriving to target, was studied. Moreover, with a ridge filter modulator, Spread-Out Bragg peaks (SOBPs) were obtained with a width up to 3,4cm and a uniformity of 98,5 %.

The MC model produced in TOPAS was first benchmarked against a 150MeV proton beam in air. Secondly, the experimental data of the large fields were compared with the simulated ones. The simulation of depth-dose distributions and lateral beam profiles agreed with the experimental data. Furthermore, the model was used to estimate the number of initial protons required to achieve an experimental dose and to estimate the location of the Bragg peaks.

All in all, the dual-ring passive scattering setup has been successfully implemented and is ready to be used to perform radiobiological experiments. Also, the TOPAS MC model can be used to assist in the preparation of these experiments and to further optimize the beamline design.

Preface

This report is the result of my master thesis project and concludes my Master of Science in Biomedical Engineering studies at the Delft University of Technology in Delft, The Netherlands. This work was developed within the Research & Development department of Holland Proton Therapy Center (HPTC), in close collaboration with the Medical Physics & Technology section of the Radiation Science & Technology department of TU Delft.

I would like to thank everyone who has been there for me these past ten months. First, I would like to express my deepest gratitude to my supervisors. To Danny Lathouwers, who always provided valuable feedback and suggestions in our progress meetings and helped me focus on this work when it felt like there were too many things around me. To Marta Rovituro, who gave me the chance to work on this amazing topic and always trusted my capabilities. I learned so much from you these months.

I want to thank Atia Ibrahim, for being an amazing thesis partner and friend. I lost count on how many times I asked you for help and you were always there for me.

Thank you to my friends, especially those with whom I got to share the past years in Delft. To Arita, I am so glad Delft gave us a second chance. To Patricia, for supporting me when things were not so bright; I am so happy I can share with you when I am at my best. To Juls, for making me see that asking for help is also alright. To my best compiamigo, Javi. To Jacob, who even took time to correct the captions. To Josema, to Michumba, to the Edamamens, to las Musas, to the Paninis.

Finally, a special thanks to my family for being my biggest, most constant support. To Mamá for loving me no matter what. To Papá for making me see things with another perspective. To Ramón and Beatriz, for being the biggest inspiration a sister could have. When I grow up I wanna be like you.

To all of you, I sincerely thank you.

María del Henar Rituerto Prieto
Delft, September 2020

Introduction

According to the World Health Organization (WHO), nowadays about 1 in 6 deaths is caused by cancer [31]. Radiotherapy is used in more than 50 % of those patients [41], delivering high doses of radiation to kill cancer cells and shrink tumors causing DNA damage. The main challenge of radiotherapy is to distribute the dose in such a way that the target volume receives the 100% of the dose while the nearby healthy tissue is spared. However, this cannot be achieved because of the dose deposition in the surrounding tissues.

Currently, conventional radiotherapy treatment is based on indirectly ionizing photons, mainly X-rays in the energy range of 4 – 25 MeV. However, the use of ions for deep-seated tumors was explored in the 50's, showing already in 1946 a good potential of protons. The main rationale for using charged particles in radiation therapy lies in the profile of their dose deposition along a tissue depth (see Figure 1): the more the protons slow down, the higher the energy transfer to tissue. This translates into the presence of a plateau region at the entrance with relatively low dose, and a high-dose region at the end of the particle range, called Bragg peak. Figure 1 illustrates the advantage of using protons with respect to photons for deep-seated tumor: the latter will, in fact, deposit their energy mainly in the entrance channel delivering extra dose in the surrounding tissues. On the contrary, by changing the initial kinetic energy of the proton beam the Bragg peak position can be adjusted delivering the maximum dose in the tumor. Moreover, the energy modulation of the Bragg peak (Spread-Out Bragg peak) allows a dose distribution over the entire volume. Radiotherapy can therefore benefit from the proton behavior to improve the dose conformity to maximize the prescribed dose received by the tumor while sparing the surrounding tissue [33, 40].

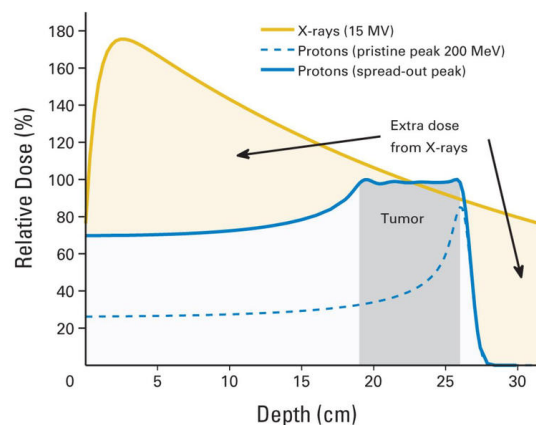


Figure 1: Comparison of relative depth-dose distributions of photons and protons. Figure taken from Mitin and Zietman [28].

The first proton therapy treatment was delivered in 1954 in the Berkeley Radiation Laboratory, a facility designed for physics experiments [33]. Nevertheless, proton therapy centers started to spread around the world only at the end of the 20th century. Nowadays, there are 104 centers around the world which have treated almost 220000 patients. In the Netherlands, there are 3 proton therapy facilities in operation [17].

Holland Proton Therapy Center (HPTC) is one of the Dutch proton therapy centers located in Delft, South of Holland. It started the first patient treatment in 2018. The facility focuses on clinical treatment, clinical and pre-clinical research. The main goal of the research program of HPTC is to show the added value of using protons, to apply research-driven proton therapy to patients and to contribute to the development of next generation particle therapy broadening the application of this treatment for different tumors indication. In order to achieve this, a better and deeper knowledge of the radiobiological mechanisms caused by protons needs to be acquired. For this reason, dedicated experimental rooms are key to perform pre-clinical research on this topic.

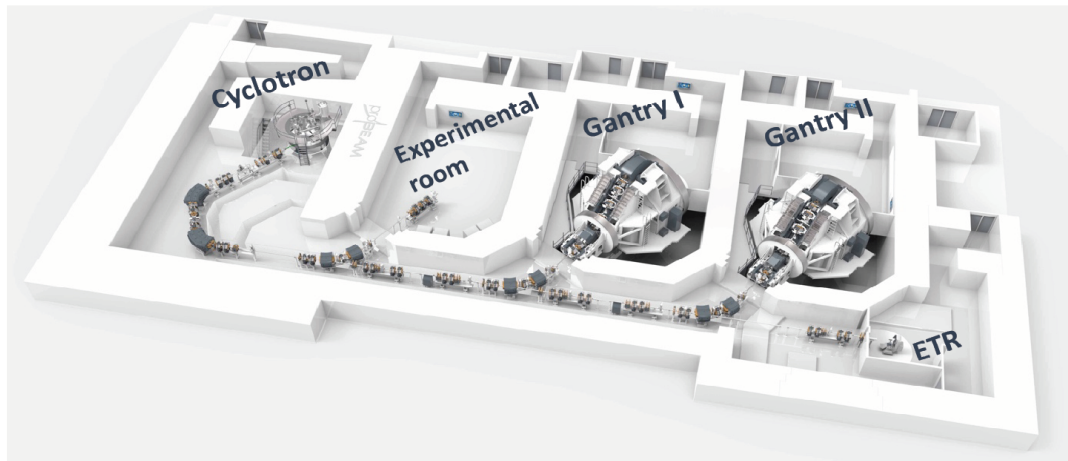


Figure 2: Scheme of the cyclotron transporting the proton beam into the four rooms in the HollandPTC: the experimental room, the two treatment rooms (Gantry I and Gantry II) and the eye treatment room (ETR). (Courtesy of Varian).

HPTC is a Varian center, where the cyclotron serves 4 different rooms: two clinical gantries, one eye treatment room and one experimental room (Figure 2). The purpose of the experimental beamline is to perform both physics and radiobiological experiments, including animal irradiations. In order to conduct all the different types of pre-clinical experiments, the beamline has to be equipped to provide large field irradiation with precise dose characterization [46]. **The first goal of this work was to implement a passive scattering system in the experimental room of HPTC to produce homogeneous fields of different sizes for various applications.** The focus of this work was to optimize the passive system for a mono-energetic 150 MeV proton beam able to:

- Irradiate a field of at least $10 \times 10 \text{ cm}^2$ with a lateral uniformity higher than 97%.
- Achieve SOBPs with a modulation width of at least 3 cm and uniformity higher than 98%.
- Conform the lateral spread using collimators obtaining a homogeneous lateral dose with a defined penumbra.
- Have a flexible, robust and reproducible beamline for different applications.

The experimental design and implementation of the passive scattering system was supported by the use of Monte Carlo (MC) simulations. For this work, TOPAS [35] MC code (Geant4 toolkit [1]) was used to assist in the setup preparation, to evaluate and optimize the beamline elements, and to perform *in silico* verification of nozzle design [18]. As first, the pencil beam characteristics were simulated and benchmarked against experimental data. Those simulations provided the main starting point to create the passive scattering model. **The second main goal of this project was, therefore, to build a MC simulation of the HPTC passive scattering beamline able to reproduce the experimental setup.**

This work is divided in five chapters. Chapter 1 provides a research background with an introduction to the physical and biological properties of protons. Moreover, it introduces the passive scattering technique, the MC method and its implementation using TOPAS. In Chapter 2, the literature study to obtain a broad overview of the reported techniques to model and benchmark the MC simulation of passive scattering system and to select an approach for this work is reviewed. In Chapter 3, the materials and methods employed throughout the project are explained. In this part, a description of the passive beamline elements and the settings required to perform TOPAS simulations is included, together with a detailed explanation of how the experiments and simulations were carried out. In Chapter 4, results and discussions are presented. In the first part, the results on the pencil beam simulations are shown. In the second part, the passive scattering system design is presented, and the result of the beam homogeneous dose deposition is illustrated. Finally, the comparison of the MC simulation of the scattering system with the measurements is performed. In Chapter 5, conclusions on the research work and future prospects are discussed.

Theoretical Background

This chapter introduces the research background which constitutes the basis of the project. Section 1.1. introduces proton therapy and why its use is spreading. Section 1.2 summarizes the basic interactions of protons with matter. Section 1.3 discusses beam line design and its main approaches. Finally, Sections 1.4 and 1.5 focus on Monte Carlo simulations and most specifically on TOPAS [35].

1.1. Physical Aspects of Radiotherapy with Proton Beams

The design of a passive scattering beamline requires understanding the interactions of proton with matter in the therapeutic range (70-250 MeV). In this range, protons undergo two main interaction processes when traversing a medium: electromagnetic and nuclear interactions. Electromagnetic interactions include both the stopping (Section 1.1.1) and scattering (Section 1.1.2) of protons. Nuclear interactions (Section 1.1.3) are non-elastic collisions where the proton enters the nucleus and knocks out one or more constituent protons, neutrons, or light nucleon clusters.

1.1.1. Energy deposition in matter: Bethe-Bloch formulation

Incident protons collide with atomic electrons and produce ionization and excitations, losing kinetic energy that is then transferred to the atom. These inelastic collisions are the main cause for the energy deposition in a given volume by the primary beam, i.e. the dose [38]. The rate of energy loss increases as the proton slows down: a proton loses more energy the longer it interacts with the electron. This effect marks the Bragg peak appearance at the end of the range.

The theory of the stopping power describes the rate of energy loss in matter of a charged particle. Bethe and Bloch developed in 1933 a formula to describe this effect [40, 41]:

$$\frac{S}{\rho} = -\frac{dE}{dx} = \frac{4\pi e^4 Z_t Z_p^2}{m_e v^2} \left[\ln \frac{2m_e v^2}{I} - \ln(1 - \beta^2) - \beta^2 - \frac{C}{Z_t} - \frac{\delta}{2} \right] \quad (1.1)$$

The stopping power S is divided by the density of the absorber material ρ to express the energy loss rate independently of the mass. Z_t and Z_p correspond to the target and projectile mass number; m_e and e are the mass of the charge and electron, respectively. $\beta = v/c$, where v is the projectile velocity. C and δ are correction terms for relativistic and quantum mechanics effects and need to be accounted for when calculating the energy loss for very high or very low energies [30]. In the radiotherapy energy regime (70-250 MeV), the corrections can be ignored. Finally, I is the mean excitation energy of the target material. It is defined as the “minimum energy than can be transferred on average to a target atom in a Coulomb interaction between the charged particle and an orbital electron” [24]. This value is a parameter that needs to be adjusted because it cannot be calculated accurately using theoretical models. It is usually computed by fitting measured range-energy values [33]. This creates uncertainties in the energy loss computation.

From the model above, the following information about the energy loss process is extracted [30]:

- It is inversely proportional to the square of its velocity ($1/v^2$), which means that the rate of energy loss increases as the proton slows down.

- It is proportional to the density of electrons in the target, i.e. higher electron density means more Coulomb interactions.
- It depends on I , which at the same time depends on Z_t . However, the dependence is through the I^{-1} logarithm, so its effect is small.

Figure 1.1 shows the solution of the Bethe-Bloch formula in water for different projectiles [40]. As the projectile Z gets higher, the maximum energy transfer occurs at a higher energy. Also, as the particle kinetic energy decreases, the energy loss increases.

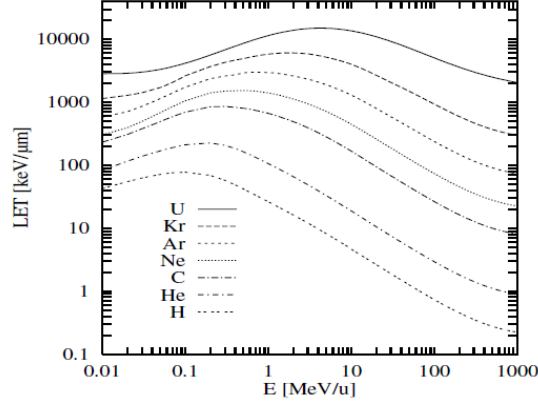


Figure 1.1: Solution of the Bethe-Bloch formula for different projectiles in water target. LET corresponds to the linear energy transfer (ratio of the energy lost by the particle, between points x and dx , divided by the path element dx), which is approximated as the material's stopping power. Figure taken from Rovituso [40] as a courtesy of U. Weber, GSI, Darmstadt.

Furthermore, the range of a charged particle is known as the “mean range”. It is defined as the depth in a medium, or total path length of a trajectory, that a charged particle with a kinetic energy E needs to traverse before it comes to rest [30]:

$$R(E) = \int_0^E \left(\frac{dE'}{dx} \right)^{-1} dE' \quad (1.2)$$

where $-dE/dx$ stands for the stopping power. Although the energy loss as a function of the penetration depth is a single value, the Bragg peak of a monoenergetic beam, i.e. pristine Bragg peak, is not sharp. This is because the energy loss is the result of many interaction that are affected by statistical fluctuation. This results in a broadening of the peak, which is referred to as “energy straggling” or “range straggling”. This means that particles with the same initial energy have slightly different ranges.

Finally, the dose deposited in a tissue is the most important quantity in radiotherapy applications [41]. The ICRU defines it as the “mean energy dE deposited by ionizing radiation in a mass element dm ”, in $\frac{J}{kg}$:

$$D = \frac{dE}{dm} \quad (1.3)$$

1.1.2. Lateral beam spread: Multiple Coulomb Scattering

The lateral beam spread is caused by the elastic Coulomb interactions between protons with the target nuclei. These interactions are referred to as “Multiple Coulomb interactions” (MCS) and cause the protons to deflect from the beam axis when multiple interactions occur. This effect is fundamental in proton therapy because, first, it influences the beam lateral penumbra. Second, MCS is the key to the functioning of passive scattering scattering systems, which use scatterers to achieve a large and homogeneous beam.

The challenges behind creating a theory describing the MCS are twofold [33]: first, to predict the exact form of the MCS angular distributions; second, to predict the width of the MCS distribution as a function of the energy and the material properties. Molière's theory [29] was developed in 1948 and it reproduces well the form of the angular distribution of MCS. This theory approximates the angular distribution as a Gaussian function (this is accepted for radiotherapy purposes [33]) and a single scattering tail. The Gaussian core approximates

the form of 98% of the scattered protons. This approximation comes from the Central Limit Theorem, according to which the distribution of the sum of many small deflections tends to a Gaussian. However, around 2% of the protons corresponding to large single scatters in the target cannot be approximated by the Gaussian core. This case is better described by the Rutherford's law [15].

The standard deviation of the angular distribution of the MCS presented by Molière can be approximated, for a small scattering angle, by a Gaussian function using the Highland formula (1975):

$$\theta_0 = \frac{14.1 \text{ MeV}}{pv} z \sqrt{\frac{L}{L_R}} \left[1 + \frac{1}{9} \log_{10} \left(\frac{L}{L_R} \right) \right] \text{ rad} \quad (1.4)$$

Where L and L_{rad} are the thickness and radiation length of the target material, respectively. L_{rad} can be found in tables for many materials [30]. L_{rad} is inversely proportional to the Z of the target, which showcases the importance of scatterer material on beam spreading: a high- Z material will scatter with a larger angle than a low- Z material, for equivalent thicknesses. Concerning the projectile, p is the projectile momentum and v its speed. z is the charge of the projectile. Highland's formula, therefore, shows the dependence of the scattering angle with the proton energy and the scattering material.

1.1.3. Nuclear interactions

Nuclear interactions are less common than electromagnetic ones but need to be accounted for as well. They are non-elastic collisions in which the protons collide with the nucleus and release secondary particles, such as protons, neutrons, gamma-rays, recoiling residual nucleus and heavy fragments, in motion. The protons need to have enough energy to overcome the Coulomb barrier of the nucleus, which depends on the atomic number of the target atoms.

Nuclear interactions in the therapeutic energy range cause a small decrease in the deposited dose by primary protons because they are removed from the beam. Figure 1.2 shows how this effect by the nuclear reactions from the entrance to near the range end. This is compensated by the liberation of secondary particles, typically with large angle scatter and short range, that deposit their energy further down the beam [15, 33].

Secondary neutrons produced by nuclear interactions are very penetrating in tissue. There are reports that secondary neutrons might increase the risk of secondary cancers or late effects in patients [41]. However, the secondary particles produced due to nuclear interactions typically scatter with large angles from the beam axis, as opposed to primary protons. This means that if the beam-shaping element is placed far away from the target, the secondaries might clear out from the beam before entering it [33]. Additionally, in a passive scattering system with beam-shaping elements in the way, the nuclear interactions with the material also result in secondary neutron production which might reach both the target and the exterior.

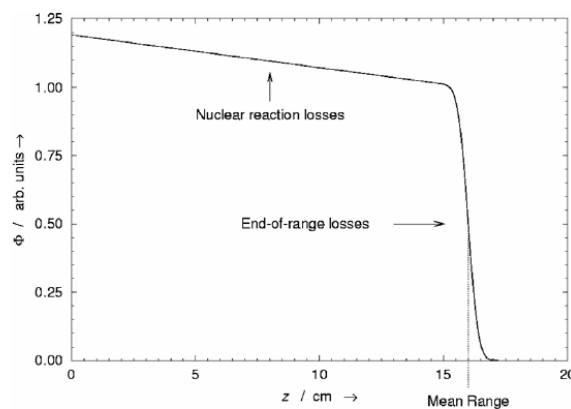


Figure 1.2: Proton fluence ϕ in relative units from a broad beam of protons remaining as a function of depth z , in water. The nuclear reaction causes the loss of protons from entrance to near the end of range, while the end-of-range losses are caused by ions rapidly losing energy and being absorbed by the water. Figure taken from Gottschalk [15].

1.2. Biology of Therapeutic Proton Beams

The goal of proton therapy is to eradicate malignant cells while maintaining the normal tissue complications as low as possible. It is widely accepted that the critical target molecule in cancerous cells of ionizing radiation is deoxyribonucleic acid (DNA).

The DNA molecule contains genetic information and is composed of two condensed strands that coil around each other. DNA has multiple ways to repair itself from radiation; however, the damage on this molecule is directly related to cell death. The three main mechanisms of DNA radiation damage are: single strand break, double strand break (DSB) and loss of a base [40]. Figure 1.3 depicts these mechanisms.

The number of DSB usually increases linearly with dose. However, the effect of radiation induced damage not only depends on the deposited dose but also on the spatial distribution of the energy deposition. The proton dose deposition is governed by the stopping power, which is equivalent to the Linear Energy Transfer (LET). LET is defined as the energy released per micrometer [23]. Protons have a low dose deposition at the Bragg peak entrance, which translates into a lower LET. Then, they undergo a rapid LET increase at the range end, where most of the dose is deposited. Therefore, protons are considered as high-LET radiation because they have a high-density energy deposition along their tracks. Thus, the probability of correlated nearby DNA damages, such as SDB and DDB, is higher [41].

Protons interact with atoms or molecules in the medium through Coulomb interactions. These events liberate electrons that further interact with the medium and scatter elastic or inelastically. When the interaction is inelastic, there is energy deposition. If the electron is at the end of its electron track, the energy is lower than 50 eV and this event causes an excitation. If the energy is higher, ionization dominates, liberating more electrons. The reason why there is a high density of ionization events is that the mean free path of electrons in water is of few nanometers. Since the opposite DNA strands distance 2 nm, the probability of high local damage in the form of DSB occurring is high [40, 41]. This clustering of radiation damage is assumed to cause the effectiveness of high-LET radiation [33]. This reduces the cell's repair ability [41].

Finally, the Relative Biological Effectiveness (RBE) is used to compare the biological effectiveness of charged particles with respect to photons [40]. It is the ratio between the physically absorbed photon dose D_{ref} for a reference radiation of 220 keV for photons, between the physically absorbed ion dose D_{ion} , yielding an equal biological effect:

$$RBE_{isoeffect} = \frac{D_{ref}}{D_{ion}} \quad (1.5)$$

RBE therefore depends on the cell type and particle type, and it increases for higher LET. In clinical applications, a constant RBE of 1.1 is assumed for protons [33]. This approximation means that to obtain the same biological effect, the prescribed dose using photons is 10% higher than the one using protons.

1.3. Basis of Beamline Design

Proton therapy systems aim at depositing a homogeneous dose in a target volume, ensuring both lateral spread of the beam and uniform dose distribution longitudinally. In these systems, the protons are first accelerated in a cyclotron or synchrotron and then go through an energy selection system and a beam transport system, which leads them into the treatment or experimental room. The purpose of the beamline, which starts at the nozzle entrance, is to transport the proton beam to the target volume. Its design is key for achieving the desired dose distribution, which depends on each specific application.

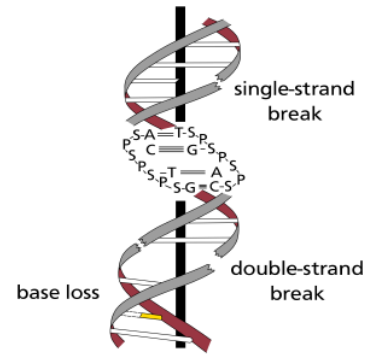


Figure 1.3: DNA molecule and the main radiation induced damage mechanisms: single-strand break, double-strand break and base loss. Both DNA strands are connected by hydrogen bonds between compatible bases. Figure taken from Rovituso [40].

The proton beam exiting the nozzle is mono-energetic and its lateral spread is a few millimeters [33]. Achieving further beam spreading can be done either by means of passive scattering or magnetic beam scanning. Scanned beams use magnets to deflect and steer the proton beam. Passive scattering techniques, on the other hand, accomplish the spreading by placing scatterers and range-shifting materials in the beamline.

Nowadays, the use of beam scanning is widely spread in the clinics due to its advantages, such as the fact that it is not target-specific or that it reduces the amount of material placed in the beamline [41]. However, this technique has difficult requirements in terms of the technological precision it requires. Therefore, experimental rooms in proton therapy centers, such as the one in the HPTC, are often equipped with a fixed horizontal beamline, with single pencil beam. In these cases, it is required to implement a passive scattering system to be able to uniformly irradiate areas and volumes. The focus of this project is on the passive scattering technique.

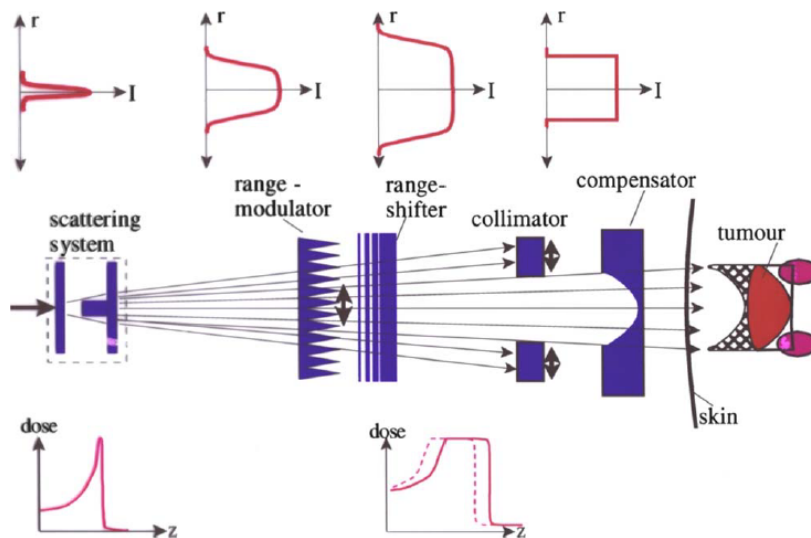


Figure 1.4: Scheme of a passive scattering system. The top row presents the lateral broadening of the beam as it traverses the beam-shaping elements. The central row includes the beamline elements (scatterers, range modulator and range shifter, collimator and compensator). The lower row showcases the beam broadening in the longitudinal direction. Figure taken from Schardt et al. [41].

1.3.1. Passive scattering technique

There are several designs of the passive scattering system to achieve beam spreading, each suitable for different applications. Its main principles and elements are grouped in three: scattering techniques, range modulation techniques and conforming techniques. Figure 1.4 summarizes the principles of these systems: a narrow beam with a Gaussian shape traverses a scattering system generating a flat transversal profile; next, the beam goes through a range modulator and the Bragg peak is spread-out in the longitudinal direction; the range shifter, collimator and compensator then help conform the spread-out beam to the target volume.

Scattering techniques

Scattering techniques are used to obtain the lateral beam spread. The most basic setup includes placing a high-Z material flat thin foil, such as lead, in the beamline. This type of material scatters the beam into a Gaussian profile with a full-width half maximum (FWHM) of a few centimeters, while maintaining a low energy loss thanks to its reduced thickness. This setup is useful for irradiating small fields requiring a sharp penumbra. However, its efficiency is low because the homogeneous region remains small due to the Gaussian-like shape. Therefore, it requires irradiation at high intensities, which produces secondary neutrons. To improve the efficiency and adapt it to other fields, there are more complex scattering systems, such as contoured scatterers and dual-ring scatterers [33]. These setups are referred to as double scattering systems, since the second scatterers are used in combination with a first flat scatterer. By optimizing their design, one can guarantee constant energy loss and appropriate scattering. Section 3.2.1 further develops on dual-ring scatterers.

The double scattering system used in this work, further presented in Section 1.4.1. is composed by a single

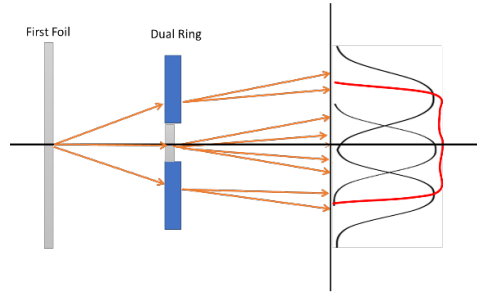


Figure 1.5: Double scattering technique using dual ring. The beam traverses the first foil and scatters towards the dual ring. Then, the generated beam profile is a combination of the Gaussian-like profile generated by the inner circle and annulus-shaped produced by the outer ring.

lead foil and a dual ring scatterer. According to Takada et al [44], this design increases beam transport efficiency by a factor of 3 with respect to single scattering.

The dual ring scatterer has an inner circular region made of lead, i.e. high-Z material, surrounded by Aluminum ring, i.e. a lower-Z material. As seen in Section 1.1.2, higher-Z materials scatter with a larger angle than those with lower Z, for the same material thickness. The inner ring produces a Gaussian-like profile while the outer ring produces an annulus-shaped profile, as presented in Figure 1.5. To produce a flat profile in the target region, the thickness of the outer ring is such that its water-equivalent thickness, is equivalent to that of the inner lead circle.

Range modulation techniques

The spreading of the monoenergetic beam in the longitudinal direction is achieved by means of a range modulator. Range modulation combines proton beams of different energies and weighted intensities to obtain a region that is uniform in depth which is referred to as Spread Out Bragg Peak (SOBP) [33] (Figure 1.6). The dose D at each point of the SOBP can be defined as follows:

$$D(x, y, z) = \sum_i w_i B_i(x, y, z) \quad (1.6)$$

where $B_i(x, y, z)$ is each Bragg curve and is the weight of each of them.

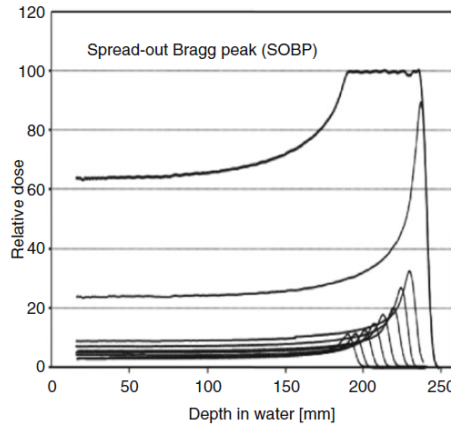


Figure 1.6: Superposition of pristine Bragg curves of proton beams with different energies and weights to generate a SOBP. Figure taken from Rath and Sahoo [38].

There are three main techniques to achieve this: energy stacking, employing range modulation wheels (RMW) and using ridge filters. Energy stacking consists in modifying the energy of the beam entering the nozzle, changing the energy usually at accelerator level. This technique is barely used because the process of switching energy layers is very slow. RMW is the most common method used in passive-scattering systems. The

wheel is composed by steps of different thicknesses and angular widths. The thickness of the step determines the range of each pristine peak; the width establishes the weight of the peak, i.e. number of protons. The wheel rotates rapidly so that the steps are irradiated sequentially when the beam is on, constructing a SOBP. Nevertheless, the passive scattering system presented in this work, as discussed in Section 1.4.1, implements a ridge filter.

Ridge filters have a more widespread use in experimental rooms because of their simplicity and because they do not need to be synchronized with the beam, as is the case for the RMW. The ridge filter is a stationary device composed by a 2D array of pins. The thickness of the pins determines the pristine peak range, while their width relates to the weight. The main drawback of the ridge filter, compared to the other techniques, is that a different device is required for each different SOBP modulation width.

Conforming techniques

Conforming techniques include placing elements in the beamline that conform the dose to the target region. Different elements can be used for this purpose, such as apertures and range compensators. These elements are target-specific and adjust the irradiated field to the target volume in both the lateral and depth directions, respectively [41].

According to section 1.1.1, high-Z materials have a higher stopping power which means that less material is necessary to stop protons hitting the aperture. However, protons might interact with the aperture walls, as shown in Section 2.2.2, perturbing the dose distribution arriving to the target area. Thus, the thicker the collimator, the larger the impact on the lateral penumbra because more interactions occur [7]. Moreover, as mentioned in Section 1.1.3, there is secondary neutron dose production caused by the nuclear interactions between the proton beam and the high-Z collimator, which may arrive to the target. Various authors ([7, 18]) address this issue by implementing a plastic pre-collimator, with low neutron cross-section, to initially stop protons and reduce the secondary dose production. This way, the pre-collimator can have a fixed dimension while the high-Z, thin collimator is adapted for different aperture sizes. Therefore, the passive scattering system implemented in this work employs a PMMA (low-Z) pre-collimator and a Brass collimator (high-Z).

1.4. Basis of Monte Carlo Simulations

Monte Carlo (MC) simulations is the most accurate and reliable method for simulating particles interaction [32, 34, 42]. It uses detailed physics models, considering the interactions particle-by-particle and step-by-step, and taking into account the nature of the particle, the energy regions, and the material [33]. This section includes a description of the MC principles for particle transport and an overview of the main MC codes.

1.4.1. Monte Carlo particle tracking and handling of secondary particles

Particle transport is a stochastic process in which energy, position and direction of each particle are independent random variables, described by probability density distributions. Each particle has a trajectory, which is called particle history, and it involves the generation of secondary particles through interactions. Using the MC methods for particle tracking involves generating many particles to obtain an appropriate accuracy. The tracking process of particle histories simulations starts at a source distribution, from which several events are sampled. The particles then go through a geometry, having information both about the physical geometry of the elements and the material composition. Each particle progress is discretized into several independent small steps. At each step, there is random sampling from one or more relative probability distribution, which are in accordance with the physics laws. At this point, the next particle interaction is chosen [33]. Figure 1.7 shows a schematic illustration of particle tracking.

To have a computationally affordable technique, not all physics interactions are modeled for charged particles using MC techniques. Likewise, the step size must be chosen determining the length in which, for instance, continuous energy loss or scattering angle is assumed [2]. Moreover, the secondary particles generated through interactions are saved in memory and then might be tracked when the primary particles tracking concludes. There is the choice of not tracking all secondary particles to reduce the computational cost. In these cases, the non-tracked particles deposit their energy locally to ensure energy conservation [33].

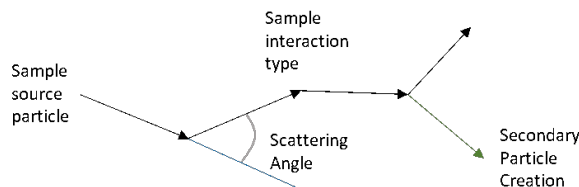


Figure 1.7: Schematic diagram of particle tracking in MC. Each line ending in arrow indicates one step. The particle scatters at different angles at each step. In the sixth step, a secondary particle is created.

1.4.2. Proton physics definition in Monte Carlo methods

The main appeal of MC simulations comes from how accurately it models the particle physics. This is done using theoretical models, parametrizations, and experimental cross section data for both nuclear and electromagnetic interactions [33]. The MC user can define the physics processes contributing to the interactions of particles in a medium, depending on the application. Nevertheless, the interaction processes modeled in MC are usually chosen to simulate as similarly as possible the experimental data.

1.4.3. Monte Carlo codes

The user needs to define input parameters when creating a MC simulation. Paganetti et al. [33] enumerated all the elements which need to be specified, including the tracking geometry, the materials that particles traverse, the physics processes or the detector responses, among others. The freedom of definition of these elements, however, depends on the MC code being used.

There are many general-purpose MC codes in use in particle therapy, such as MCNPX [27], FLUKA [12], Geant4 [1] or SHIELD-Hit [4]. Others focus on medical applications, such as VMCPPro [13], GATE (Geant4) and PTSIM (Geant4). These MC programs are either software for which the user writes the input file based on their program or an assembly of toolkit libraries organized in different functions, from which the user has to manually program the simulations, such as Geant4 [33]. Furthermore, the codes mainly differ in the possibilities they provide the user for tracking parameters control, e.g. physics settings, materials.

Developers have tried to find a trade-off between reducing the complexity and ensuring model flexibility. TOPAS, for instance, is a state-of-the-art platform layered on top of the Geant4 toolkit which allows to simulate complex processes and geometries without the need of fully understanding the Geant4 underlying processes or writing complex code. TOPAS, which was first developed for proton therapy simulations, can model any fundamental particle. Nowadays, its applications are extended to other types of ion therapy [11]. In this case, the simulations are all built with the same code, created, and benchmarked by TOPAS developers for particle therapy use [35, 45].

1.5. TOPAS

TOPAS [35] is a MC code layered on top of Geant4, which includes and extends the Geant4 Simulation Toolkit. It aims to model and simulate the interaction of particles with matter while providing a more user-friendly application for medical physicists. This tool can perform both reliable and repeatable proton simulations. TOPAS was funded by the National Cancer Institute (NIH) and created by a group of researchers led by Joseph Perl from three institutions: SLAC National Accelerator Laboratory, Massachusetts General Hospital, and the University of California.

TOPAS Parameter Control System

The TOPAS parameter control system allows to build different simulations using the same compiled code, which is built and tested by TOPAS Collaboration. The difference between one simulation and the other relies on the set of parameter files that the user inputs, which specify the geometry, the particle source, the fields, motion, scoring, graphical output and physics settings [35]. Figure 1.8 summarizes the functioning of the parameter control system. Each parameter file consists of a simple text file of one or more lines, which can include one or more parameter files at the same time. For instance, a TOPAS simulation is run as a command-line program with the name of the parameter file that includes all the rest.

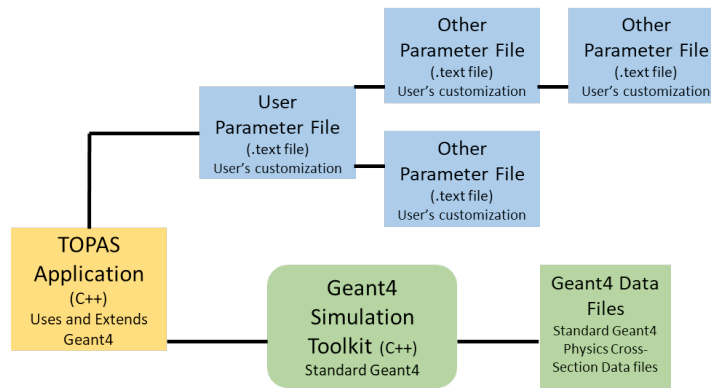


Figure 1.8: Overview of the TOPAS parameter control system. TOPAS uses and extends the Geant4 simulation toolkit (green boxes). The user writes the user parameter file to customize the simulations, which might at the same time include other parameter files. Figure adapted from Perl et al [35].

Geometry

In a MC simulation of a proton therapy system, the particles propagate through a geometrical structure. TOPAS has a set of simple geometries available, i.e. box, cylinder, and sphere, which can be combined to create other more complex structures. Furthermore, users can create any structure appearing in the standard library of Geant4 for construction of geometry solids. Furthermore, TOPAS gives the possibility to incorporate any complex component created using the Geant4 ++ geometry library into their model.

Beam source description

MC models applied to proton therapy typically start at the nozzle entrance, i.e. exit window. This means that the simulation does not include the modeling of the beam line magnets steering the beam before the exit window, or the cyclotron. Hence, the first step for creating MC models for simulating accurate dose distributions is to obtain information about the pencil beam at the nozzle entrance. A pencil beam is characterized by both its energy and optical properties [16]. Therefore, the parametrization of the beam at exit window is usually based on beam energy, energy spread, size and shape of the beam and its angular distribution [14, 32, 34, 42, 52]. TOPAS supports providing a parametrized description of the beam source. This parametrization is further described in Section 2.1.2

Physics settings

Physics lists include the physics models and processes that are related to particles and are used during the MC simulation to establish when an interaction occurs. Geant4 offers lists with models for different energy ranges, particle types and materials [1], which can be modified by the users. Moreover, TOPAS provides a set of default physics lists, referred as the “TOPAS default modular physics list”, that has been validated both for simulating clinical proton beams (Perl et al., 2012) and for proton therapy research use [25]. The TOPAS modular physics list is commonly employed in literature for TOPAS models [35, 37, 42, 45, 48, 49].

There are two parameters that need to be set to control the particle transport during the simulations: the maximum step size, i.e. maximum length that a particle traverses before a new calculation is done, and the production range cuts, i.e. limit at which a particle stops being tracked and deposits its energy locally [36]. A common approach in literature is to use TOPAS default values: production range cuts for all particles set to 0.05 mm and step size automatically selected based on local geometry and physics [35].

Scoring

The goal of performing MC simulations is to obtain outputs that provide useful information to the user concerning a given physical process. For this purpose, there are regions, i.e. surfaces and volumes, which are used as scoring regions. TOPAS provides many physical quantities which can be scored, such as the dose to a medium, fluence, surface current or linear energy transfer (LET). Furthermore, it offers the possibility of implementing filters to the scorers, based on particle type, energy or the origin volume, for instance. Moreover, TOPAS scoring can perform statistical handling, reporting values such as the mean or the statistical uncertainty of the scored quantity.

2

Literature Study

Having a reliable Monte Carlo (MC) model of a passive scattering system is a useful tool to assist in the experimental setup preparation, to evaluate and optimize the beam line elements, and to perform computational verification of nozzle design. In this chapter, we perform a literature study in which we provide a broad overview of the reported techniques to model and benchmark the MC simulations of passive scattering systems. It is divided into three main sections: analysis of nozzle design methods and how to characterize the beam entrance; benchmarking techniques used to validate the MC model; conclusions of these findings. This review constitutes a shorter version of the original study titled "Passive Beam Characterization Using Monte Carlo Techniques".

2.1. Approaches to Build a Monte Carlo Simulation for Passive Scattering Systems

This section gives an overview of relevant aspects discussed in literature for building a MC model of a passive scattering system in the following structure: first, we report how different authors model the beamline elements with different accuracy; second, we present the parameters characterizing the beam at the nozzle entrance, their influence on the model, and how they can be found.

2.1.1. Nozzle simulation accuracy

Modeling the nozzle and beam source is essential in MC simulations of a passive scattering proton system. The nozzle is defined as the set of elements placed in the beamline through which protons are delivered to the target volume. The system's manufacturer provides information concerning the geometry and composition of the beamline elements. The quality of this information, which is not always reliable or available [3, 5], plays an essential role concerning the precision with which the beam shaping elements are modeled.

Numerous authors perform a detailed model of the nozzle, down to millimeter accuracy following the vendor blueprints [8, 25, 34, 35, 45]. They specify the need to do a posteriori fine-tuning of parameters in their simulation to match the simulations to the experimental data. Several other authors ([3, 18, 47, 49, 51]) state that they model the passive beamline elements, but they do not specify how accurately.

Various authors ([5, 32, 49]) model a double scattering system following the manufacturer's blueprints, reporting sub-millimeter accuracy. They report the need to fine-tune the initial properties of the modeled beam. Both Bednarz et al [5] and Verburg et al [49] report that these uncertainties are caused by material properties, such as densities and mean ionization potentials of materials composing the beamline elements. Therefore, an accurate geometrical description of the elements can make the geometrical uncertainties negligible although other sources of uncertainties remain.

Other authors simplify the passive beam elements as much as possible. Beltran et al [6] create a simplification of the passive system and clinically test it in [22]. Their model consists of a unique lead foil designed to substitute all the other beamline elements. Following the same line, Yuan et al [52] build a Virtual Machine Source Model and then clinically test it in [53]. They state that the correctness of a model is based on whether

the simulations agree with the measurements. They create a beamline which is a close representation of the physical one in a way that the simulated results are close to the measured values.

Table 2.1: Maximum SOBPs range and modulation width differences between experimental measurements and MC simulations. The results include results reported for models of Double Passive Scattering Systems.

Article	Year	Geometry Accuracy	SOBPs Range	SOBP width
(Liu et al, 2019)	2019	Millimeter	0,4 mm	5 mm
(Perl et al, 2012)	2012	Millimeter	1 mm	2,5 mm
(Testa et al,2013)	2013	Millimeter	1 mm / - 2 mm	± 3 mm
(Verburg et al, 2016)	2014	Submillimeter	1 mm	3 mm
(Paganetti et al, 2004)	2004	Submillimeter	1 mm	1 mm
(Beltran et al, 2014)	2014	None	2 mm	
(Yuan et al, 2018)	2018	None	2 mm	2,5 mm

Table 2.1 reports the maximum SOBPs range and modulation width differences between measurements and MC simulation for significant papers following different geometry modeling approaches in terms of accuracy. All studies report maximum SOBPs range disagreement between measurements and simulations of 2 mm or less. Those studies simplifying the geometry ([6, 52]) achieve slightly less accurate agreements, with a 1 mm difference from the others studies. Studies modeling their geometry down to millimeter accuracy ([25, 35, 45]) generally achieve similar agreements than those modelling down to submillimeter accuracy. The SOBP modulation width oscillates between 1 mm and 5 mm depending on the model. The differences between agreement does not follow a pattern depending on the geometry accuracy.

Given all this, achieving the highest geometry accuracy in the nozzle geometry does not improve much the final outcome. There is a clear tendency in the research community towards creating an approximation of the system and then tuning other parameters. Literature reports how even after a beamline model achieves almost-perfect geometrical accuracy with respect to the manufacturer's blueprints, there are still present uncertainties caused by the element's composition or cross-section variations [5]. Also, the parametrization of the beam at exit window, described in the following section, introduces physics approximations to account for. Further detail on this is provided by Renner et al [39], whom perform a thorough investigation on the uncertainties arising when modeling passive scattering systems using MC techniques.

2.1.2. Characterizing the beam entering the treatment head

As it was specified in Section 1.5, the first step for creating MC models for simulating accurate distributions is to obtain information about the pencil beam at the nozzle entrance. The parametrization of the beam at exit window is usually based on its energy and optical properties: beam energy, energy spread, size and shape of the beam and its angular distribution [14, 32, 34, 42, 52].

Lateral spread and angular spread

The angular spread distribution and the spatial spread beam distribution, also referred as beam divergence and lateral spread respectively, are optical properties of the beam. The angular spread distribution can be defined as the variation in beam spot diameter as a function of the distance to the target in an experimental scenario. The lateral spread, sometimes defined as one standard deviation of the Gaussian spot at exit window [16], can be obtained experimentally from ionization chambers placed at the entrance of the treatment head, measuring the beam spot size [5, 14, 32, 47]. Figure 2.1 shows the effect of beam divergence on the spot size as a function of beam depth in an example pencil beam.

Grevillot et al [16] measure both parameters experimentally for a Pencil Beam Scanning (PBS) system: first, they compute the spot size by measuring the dose profiles using a scintillating screen coupled with a CCD camera, at different distances going from the nozzle exit to past the isocenter position, i.e. beam envelope. Second, as the spot size varies linearly as a function of distance, they compute the slope of the linear fit for each energy, which is the divergence of the beam and also allows computing the spot size at the exit window. The lateral beam profile after traversing the passive scattering system beamline elements will therefore highly depend on the initial estimates for these values [45]. Section 2.2.1 further develops on how to tune lateral and angular spread to achieve good results.

According to Paganetti et al [32, 34], the lateral and angular spread accuracy is not essential in depth-dose

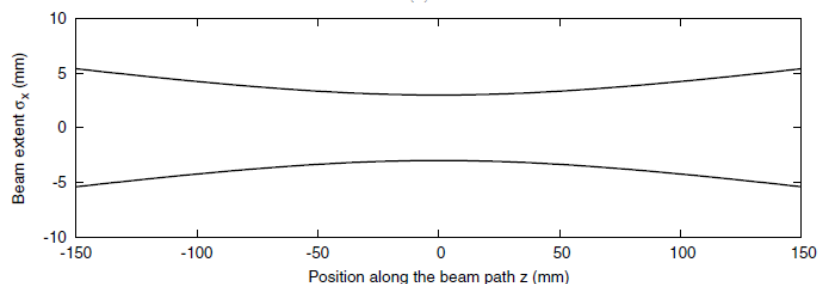


Figure 2.1: Schematic illustration of the beam size variation (σ_x) along the beam axis in depth direction (z), due to beam divergence for a pencil beam. Figure adapted from Grevillot et al [16].

distributions of passive scattering systems when kept within realistic boundaries. Figure 2.2 shows how varying the lateral and angular spread within reasonable values using a MC model of a single passive scattering system has a negligible effect on the Bragg curve [32]. Moreover, Bednarz et al [5] and Baradaran-Ghahfarokhi et al [3] report that changes in the spot size do not influence the SOBP uniformity either, when kept within reasonable values.

Beam energy and energy Spread

The energy spectrum of a proton therapy system can be considered Gaussian, with a mean energy E and an energy spread ΔE . Both properties are independent of the optical properties [16], and they are often not known with sufficient accuracy so its tuning is necessary [32]. The beam energy is linked to the proton range in water and knowing the energy spread is essential because it contributes to the finite width of the Bragg Peak [32]. Furthermore, the energy spread is specific of each system because it depends on the settings of the beam shaping slits in the energy selection system at the exit of the cyclotron, the beam absorber and the beam steering magnets [5].

According to Paganetti et al [34], the initial energy spread influences the width of Bragg peak, distal penumbra, i.e. the distance between the 80% and 20% dose levels, and peak-to-plateau ratio. Increasing the energy spread broadens the pristine peaks and decreases peak-to-plateau ratios ([3, 5, 32]). Figure 2.2 shows the effect on the depth-dose profiles of modifying the energy spread in the simulations of a single passive scattering system [32]. Furthermore, concerning the SOBP uniformity in a passive system, Bednarz et al [5] show that varying the energy spread does not have much influence when the variations are kept on a reduced range. Baradaran-Ghahfarokhi et al [3] report that beam energy and energy spread are the parameters with the largest impact of the range and peak-to-plateau ratios. Section 2.2.1 further develops on how to tune energy and energy spread to achieve good results.

The beam energy spread is found empirically by comparing the simulated pristine Bragg peaks with measured depth-dose distributions and tuning the energy spread to find the best agreement [14, 25, 32, 34]. Grevillot et al [16] and Fracchiolla et al [14] find the energy spread values of the PBS system for each energy following the mentioned empirical approach. Doing this, they arrive to a third-order polynomial function that fits the energy spread curve at the exit as a function of the energy. Paganetti et al [34] follow the same approach and find a formula that describes the energy spread as a function of the energy. Bednarz et al [5] assume a decreasing linear relationship between beam energy and energy spread. According to the authors, this is an approximation because this relationship can only be known with around 20% uncertainty due to the difficulties to measure the energy spread experimentally.

2.2. Benchmarking Monte Carlo models using experimental data

Benchmarking studies consist in comparing the outcomes of the measurements with those of the simulations, with setups as simple as possible to avoid discrepancies due to geometrical factors. This section describes the main techniques employed in studies benchmarking double passive scattering systems: using pristine Bragg peaks, spread-out Bragg peaks (SOBPs) and lateral profiles.

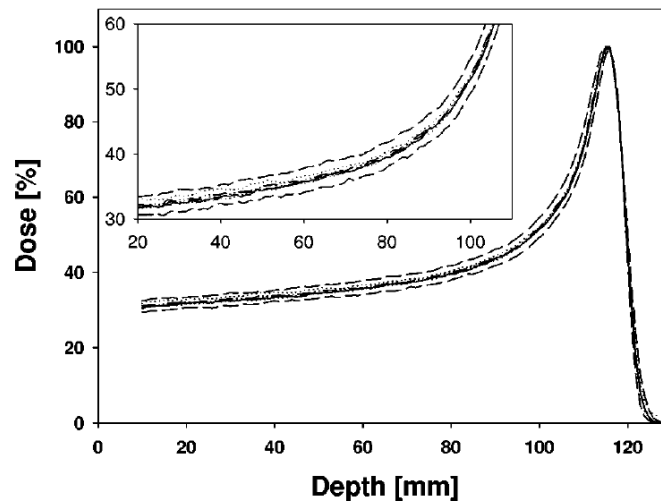


Figure 2.2: Simulated Bragg curves for a nominal energy of 150.025 MeV for a single scattering system. The solid line presents the results when using realistic initial beam parameters. Dotted lines and dashed-dotted lines represent the influence of changing the beam lateral spread and the angular spread within reasonable values, respectively. Dashed lines show the effect of modifying the energy spread from 0.45% to 0.85%. The figure on top is the result of magnifying the 2cm-11cm region. Figure taken from Paganetti et al. [32].

2.2.1. Pristine Bragg peaks and SOBPs

Pristine Bragg peaks are the depth-dose curves resulting from a mono-energetic proton beam travelling through a medium. The main goals for using them for benchmarking a MC model are: validate the beam source, geometrical model and physics model details used in the MC code [9, 25, 45]; determine the initial beam parameters [9, 32, 52]; verify whether the model beam energy is consistent with the actual one [45, 52].

SOBPs are the combination of proton beams of different energies and weighted intensities ideally, resulting in a uniform dose in the longitudinal direction of the beam. The process to produce them is described in Section 1.3.1. The aims of benchmarking the SOBPs are: evaluate the consistency of the range modulator geometry implementation [25, 32, 47], the beam current modulation and analyze the time-dependent behavior [45].

Experimental measurements setup

Nowadays, water phantoms are widely used for performing experimental measurements of depth-dose curves. They are composed by a water tank and mainly two ionization chambers (IC): the first one is a parallel-plate IC fixed at the entrance of the water tank; the second IC is inside the water tank, usually attached to a linear stage that moves it to different depths. Then, for every position, the number of incoming protons is registered by the first IC and the number of protons after a certain depth in water are counted by the second IC. The Bragg curves are obtained by plotting the ratio of the two values provided by the different chambers as a function of the depth position.

Literature reports the use of different ionization chambers, such as the PPC05 parallel plate ionization chamber [3, 25], the Markus ion chambers [3, 32, 37, 42, 45], or the CC01 ionization chamber [47]. Piersimoni et al [34, 52]. Moreover, in those cases where the range modulation wheel (RMW) cannot be removed from the beamline, it is kept static to only obtain the Bragg peak with highest weight.

Simulations setup

The scoring setup for simulating the depth-dose measurements usually simulates the water phantom, consisting of a water tank of similar dimensions as the experimental one [25, 34, 42, 45, 47, 52] and a scoring volume. The deposited dose is computed in the phantom medium along the central axis of the beam, integrating the dose over the scoring volume diameter.

Literature differs on how the dose is computed along the axis and on the modeling of the scoring volume. Some models design scoring volumes that mimic the sensitive area of the ionization chamber: Paganetti et

al [32] design the scorer so that it resembles the Markus chamber, Liu et al [25] the PCC05 and Tommasino et al [47] the CC01. On the other hand, others integrate the dose over a larger transversal area than the ionization chamber [35, 37, 42, 45]. There is a trade-off to consider regarding this choice: a larger scoring diameter allows obtaining better statistics for a lower number of simulated primary histories; however, a smaller one provides better peak localization in the transversal plane.

Results

The benchmarking process is usually performed in both pristine peaks and SOBPs. Some studies ([6, 35, 42]) perform benchmarking only on SOBPs, with no pristine Bragg curves benchmarking. The main disagreements appearing between measured and simulated depth-dose curves are in range and distal fall-off, i.e. the difference between the distal 80% point and the 20%. In the SOBPs, the modulation width and flatness also show discordance [35, 45].

Usually, the benchmarking process of depth-dose curves consists in tuning the four beam source parameters described in Section 2.1.2: energy spread, mean energy, lateral spread, and angular spread. However, literature presents different approaches to reach consistency among experimental and MC measurements.

Tommasino et al [47] find the exit beam parameters in air experimentally, i.e. pencil beam with no beam shaping elements in the beamline, using it as input values into the double scattering simulations. Paganetti et al [32] use a single scattering beamline to benchmark their pristine Bragg peaks instead, although their system is a double scatterer one. Then, they adjust the energy spread of the beam empirically to match the experimental Bragg curves. The authors report that the energy spread values provided by the manufacturer are only estimations based on the beam line optics and are 5 to 20% lower than those found empirically. Moreover, they use the nominal energy given by the Treatment Planning System (TPS) as default energy.

On the other hand, numerous authors ([3, 25, 37, 45]) benchmark the Bragg peaks with the main double passive scattering beamline elements on the way. In most cases, the RMW is kept static to only obtain the most distal Bragg peak. This is the peak with the highest weight and therefore the one impacting the SOBP the most. Then, each double scattering setup goes through a process of tuning beam parameters to achieve the Bragg curves agreements. They specify this is necessary based on either having an imprecise knowledge of materials composition of the elements or because the uncertainty on the measured initial parameters is high. Different studies disagree on how to perform this fine-tuning:

- Paganetti et al [34] and Liu et al [25] find an agreement by tweaking mean energy and energy spread alone. Furthermore, Liu et al [25] state that the lateral and angular spread influence is almost negligible when reasonable values are provided for a double scattering model.
- Testa et al [45] perform an experimental validation of the TOPAS. The authors report having an imprecise knowledge of materials composing the nozzle. Thus, they perform energy tuning directly on SOBPs to improve their flatness, modulation width and range. Figure 2.3 shows depth-dose curves of measurements compared to MC simulations before and after performing the energy correction. Moreover, the authors tune the angular spread because the manufacturer values are inaccurate.
- Prusator et al [37] tune mean energy, energy spread, spot size and angular spread to overcome the sources of uncertainties coming from the difficulty of measuring these parameters. Furthermore, the authors report that for configurations meant to achieve large fields, as the requested energy is lower, the distal fall-off of the curves cannot match by just tuning these parameters. They hypothesize that this is caused by the presence of more material in the beamline introducing further uncertainties. To achieve distal agreement they adjust the thickness of the first scatterer in the simulations.
- Baradaran-Ghahfarokhi et al [3] perform a sensitivity analysis on their double passive scattering system. They find agreement by modifying the energy spread and energy and report that the energy spread is the parameter providing the largest sources of uncertainties. They also find the spot size has almost no influence on the pristine peaks. Moreover, they tune the first foil scatterer thickness within manufacturer tolerances to find range agreement for configurations achieving larger lateral fields, pointing out the small effect on profile flatness and symmetry of these modifications.

Table 2.2 summarizes the results reported by the above-mentioned studies following different beam source parameter tuning. The disagreements between experiments and simulations that lead to parameter tuning

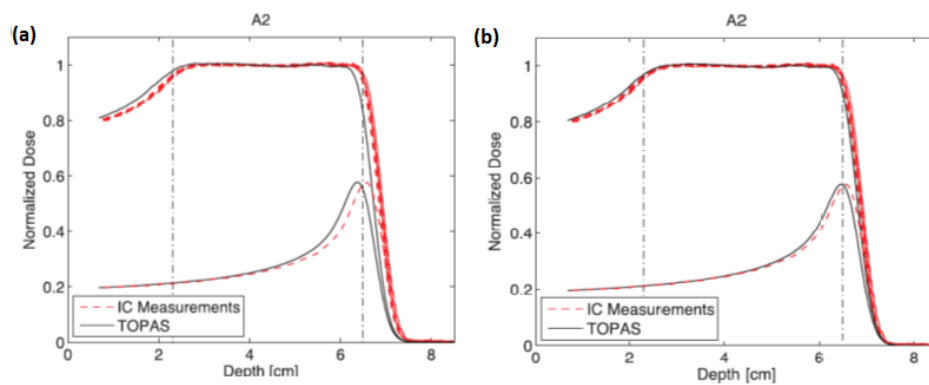


Figure 2.3: Depth-dose curves of ion chamber measurements compared to TOPAS measurements for SOBPs and most distal pristine peaks. (a) Original curves before tuning any parameters, (b) Result of increasing the energy of the proton source by a value leading to a +1 mm water equivalent range. Figure from Testa et al [45].

Table 2.2: Maximum distances between measurements and simulations for the pristine Bragg peaks (d_{90} , i.e. the depth of penetration at the distal 90% point of the peak) and SOBPs (d_{90} , modulation width, i.e. distance between the proximal 90% and distal 90% isodose levels). An x in the last five columns indicates that a parameter is tuned (E : energy, ΔE : energy spread, LS: lateral spread, AS: angular spread, FT: first foil thickness). A gray square means that a given value is not reported.

Articles	Pristine d_{90}	SOBP d_{90}	SOPB width	E	AE	LS	AS	FT
[25]	0.03 cm	0.04 cm	0.5 cm	x	x			
[37]	0.1 cm	0,1 cm	0.3 cm	x	x	x	x	x
[3]	0.1 cm	0.1 cm	0.2 cm	x	x		x	x
[45]		0.1 cm / - 0.2 cm	± 0.3 cm	x			x	
[32]		0.1 cm	0.1 cm	x	x			

are often caused by inaccurate knowledge of the materials and geometry of the beamline elements [45, 52], or approximations in the model [52]. Also, the difficulties in measuring the beam parameters used in the MC models [37], or having experimental estimations that are not accurate enough [3, 32, 45], produce uncertainties that are overcome by parameter tuning. Based on the reported results, one cannot choose a set of parameters that should be tuned for every application: the tuning procedure is highly dependent on the experimental setup, its model, and the initial parameters estimates available.

2.2.2. Lateral profiles

Beam lateral profiles measure the spread of the scattered proton beam in the lateral direction. Their analysis is mainly used in the benchmarking process to test the correct simulation of the double scattering system as a whole [32], allowing to verify the modeling and positioning of the collimators along with the accuracy of the multiple scattering physics model implemented [25, 32].

Experimental measurements setup

Literature reports four main ways for acquiring experimental lateral beam profiles:

- Using diode detectors placed in a scanning water phantom (IBA Dosimetry [25]) (Scanditronix EDP 2 [6]) (PTW 60020 [37]) (diode edge detector [3]).
- Employing ion chambers with a high resolution in a water tank [45, 52]. Testa et al [45] employ the MatriXX detector, which is a square grid of ion chambers, to obtain the complete 2D dose map for a plane perpendicular to the beam direction.
- Performing irradiation of a large-area EBT3 film in air at the beam isocenter [47].
- Using a scintillating screen coupled to CCD-cameras (Lynx), placed at target position [47].

The first two methods directly output dose profiles. The third one requires a calibration process to convert to dose values. The last one, on the other hand, outputs pixel intensity.

Simulations setup

The most common approach in the MC simulations to obtain the lateral profiles is to model a detector mesh in the cross-field profile with a low resolution of around 1 mm in the profile direction [6, 25, 47, 52]. The scorer is usually placed in water [32, 52] although this is not always indicated.

Results

The beam lateral profiles are usually benchmarked at different positions and for different nozzle configurations and settings of the system: for different modulations widths and energies, for apertures of different sizes, or for different regions of the SOBP.

Liu et al [25] construct and commission a double scattering passive system and compare its dose computations to TPS. The authors benchmark one configuration of the system, modifying the aperture sizes. Prusator et al [37] model and benchmark the different beam line configurations, which achieve different ranges and SOBP width, of the Mevion S250 scattering system; each of these configurations has different apertures and air gaps. Beltran et al [6] benchmark the simulation with measurements using only one aperture size; however, to further verify their system, they evaluate differences between TPS and MC for different apertures and compensator combinations.

Some authors benchmark profiles at different depths of the SOBP depths to evaluate different beam spot sizes and validate the physics model [6, 25, 37]. Others, e.g. Yuan et al [52], only compute it at the center of the SOBP. Some do not specify the region of the SOBP at which they evaluate the differences and the reader needs to guess this position [32, 47]. Figure 2.4 shows examples of lateral profiles computed for different aperture sizes and at different depths of the SOBP. In Figure 2.4 - a), one can observe the “horns” appearing at the volume edges at the entrance of the aperture. This showcases a correct modeling of the slit scattering effect, which is caused by electromagnetic interactions. This effect is due to the increased proton fluence surrounding the edges because protons interact with slit surfaces of an aperture, losing energy and scattering mainly towards the beam axis [25]. In Figure 2.4 - b), however, the horns are not visible anymore; this is because the slit scattering effect is negligible at the end of the SOBP.

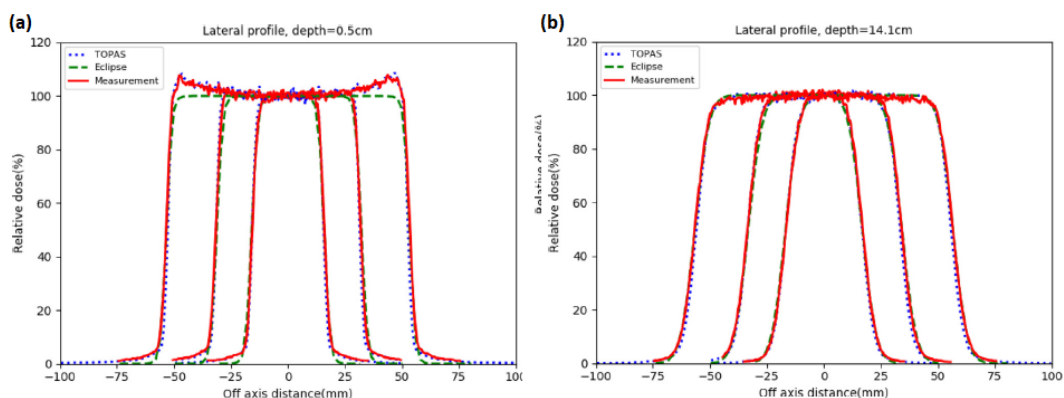


Figure 2.4: Lateral dose profiles for different aperture sizes (10x10 cm, 6x6 cm, 3x3 cm) at (a) 0.5 cm depth, (b) 14.1 cm depth computed using TOPAS, Eclipse (TPS) and experimental measurements Figures taken from Liu et al. [25].

Table 2.3 summarizes the results obtained for the different studies mentioned in this subsection. Their outcomes are similar: in terms of lateral penumbra, i.e., the distance between the 80% and 20% dose levels, and the full width at half maximum (FWHM), the agreement between measurements and simulations is always achieved within 2 mm. Differences in uniformity are not so commonly reported values, so a relevant comparison is not possible. Furthermore, some authors ([34, 47]) do not report numerical values to measure the agreement between measurements and simulations. This complicates the comparison between models or the reproducibility of the experiments.

Table 2.3: Maximum distances between measurements and simulations for the lateral profiles. Lateral penumbra is the distance between the 80% and 20% dose levels, FWHM is the full width half maximum, the uniformity is the flatness, and the symmetry is with respect to the center value. A gray square means that a given value is not reported.

Articles	Lateral Penumbra	FWHM	Uniformity	Symmetry
[25]	<1 mm			
[37]	<1 mm	<2 mm	<1 %	<1.3 %
[6]	<1 mm			
[47]				
[52]	<2 mm	<2 mm		
[32, 34]				
[45]			±3%	
[3]	<1 mm		<2,18%	<0,6%

2.3. Literature Study Conclusions

Applying Monte Carlo (MC) techniques to create models for passive scattering systems is useful for fine-tuning the elements that shape the beam and to verify the nozzle design for different purposes. The main goal of this literature review was to provide a broad overview of the reported techniques to model and benchmark the MC simulation of passive scattering systems. The information on this study can help find the best approach to create the MC model of the passive scattering beamline in the experimental hall of the HPTC.

First, this literature study reveals that Geant4 and TOPAS are the most common MC codes for modeling passive scattering systems, with all but 6 of the reviewed papers using either Geant4 or TOPAS as their MC code. Considering its purpose and the time constraints, the MC model of the passive beamline in the HPTC is performed using TOPAS, which ensures model flexibility while having a lower complexity than Geant4.

Second, this work concludes that the geometrical accuracy with which a system is modeled does not exempt it from the need of fine-tuning the model beam source parameters. It does not improve the final quality of the model either. Based on this, it is decided that obtaining perfect accuracy in the experimental HPTC beamline model is not a goal. Moreover, passive scattering system models usually start at the nozzle entrance. The four parameters defining the pencil beam source characteristics are the following: mean energy, energy spread, angular spread and lateral spread. The precision of these parameters has a great influence in the system's outcome. The initial beam parameters of the HPTC beamline are rough estimates, so they need to be fine-tuned first by comparing experimental and simulated Bragg curves of the pencil beam.

Third, the procedure for benchmarking a MC model is mainly based on the analysis of depth-dose distributions and lateral profiles of both measurements and simulations. This benchmarking procedure is employed for benchmarking the experimental HPTC beamline model. In this case, only the mean energy is provided as an initial beam parameter estimate; the other parameters are found by running several simulations changing the beam parameters and comparing the simulations with the measurements.

All in all, it can be concluded that the techniques to model and benchmark MC models of passive scattering systems are widely presented in literature, and that all of them follow a similar approach. However, the research community could benefit from guidelines concerning how to tune the beam parameters or how to present the final outcomes of the model. Also, there are many applications that confirm how useful these models are in an experimental environment such as the HPTC.

3

Materials and Methods

In this chapter, the materials and methods are presented. First, the facility and the setup of the passive scattering system of the HPTC experimental beamline are described, along with the experiments to characterize the passive fields. Second, we outline the TOPAS model and the MC simulations performed to characterize the pencil beam source parameters. Then, we show the methodology to do passive scattering simulations that are used to benchmark the model with experimental data.

3.1. The HollandPTC Proton Therapy Center

The project was performed at the proton therapy center HollandPTC in Delft, Netherlands. This is one of the three Dutch proton therapy centers and it focuses on both clinical treatment and research. This facility was founded as a consortium between Erasmus Medical Center (EMC), Leiden Medical Center (LUMC) and Technical University of Delft (TUD) with the focus on establishing the added value of proton therapy in respect to conventional radiotherapy. The first cancer patients were treated in September 2018.

The Varian Medical Systems cyclotron of HPTC serves 4 different rooms: two clinical gantries, one eye treatment room and one experimental room (Figure 2). The experimental part of the project took place in the latter, shown in Figure 3.1. Therapeutic proton beams are produced by the Varian ProBeam isochronous superconducting cyclotron with energies between 70 MeV and 240 MeV.

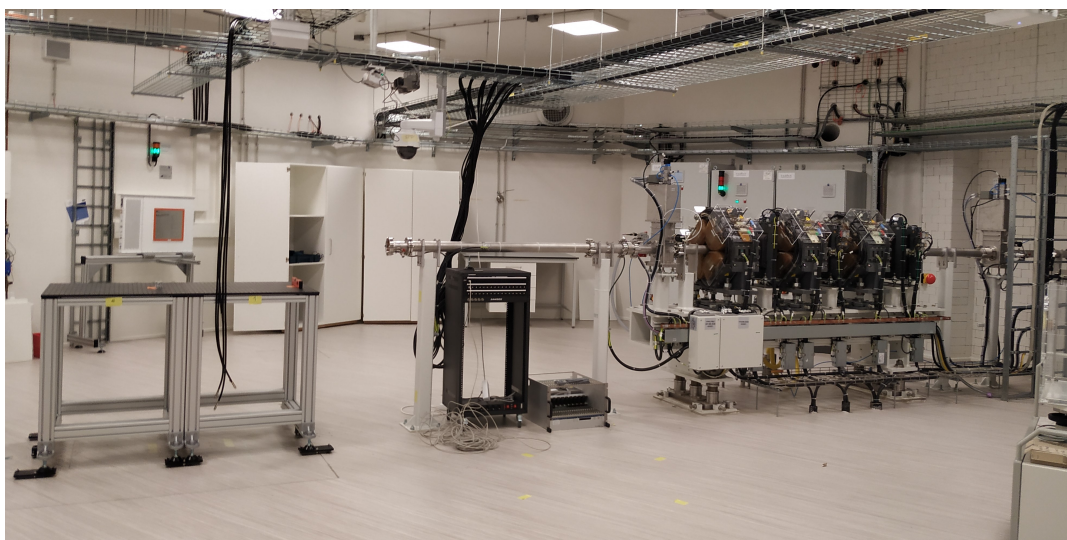


Figure 3.1: Experimental room of HPTC

The cyclotron accelerates protons to a fixed maximum energy (e.g. 250 MeV). It contains a proton source in the center of the cyclotron and a magnet which bends the trajectories of the particles into a circular orbit and

allows the cyclotron to be compact. A radiofrequency (RF) system provides electrical fields that accelerate the protons. The cyclotron is called isochronous because each proton takes the same time to make one orbit, independently of the orbit radius or proton energy. The RF system operates at a constant frequency. The cyclotron extraction system leads the accelerated protons to the Energy Selection System. The latter is composed by slits made of graphite, of variable thicknesses, which degrade the beam down to 70 MeV and allow choosing the energy spread. Finally, the Varian Beam Transport System guides the beam to the treatment rooms and the experimental room, by means of bending and focusing magnets, which arrives as a pencil beam [33, 38, 43].

3.2. Experimental Setup

The goals of the experiments carried out in this master project were to design a passive beamline for radiobiological applications, optimized for a 150 MeV mono-energetic initial beam, and to supply data to benchmark MC simulations. In order to do this, TOPAS MC simulations initially focus on reproducing the experimental data concerning the pencil beam properties. However, the latter experiment was not within the scope of this project and only the processed data have been used to validate the TOPAS simulations. The dual ring passive scattering system was implemented afterwards.

3.2.1. The passive scattering system at HPTC bunker

The experimental room in HPTC has a fixed horizontal beamline, with a single pencil beam. The purpose of this beamline is to perform both physics and radiobiological experiments, including animal irradiations. In order to conduct all the different types of pre-clinical experiments, the beamline has to be equipped to provide large field irradiation with precise dose characterization [46]. The choice of HPTC was to implement a dual ring passive scattering system (see Section 1.3.1) to have different field sizes for different types of applications. Throughout this work, the dual-ring passive scattering system was optimized for a 150 MeV mono-energetic initial beam. The complete setup is depicted in Figure 3.2.

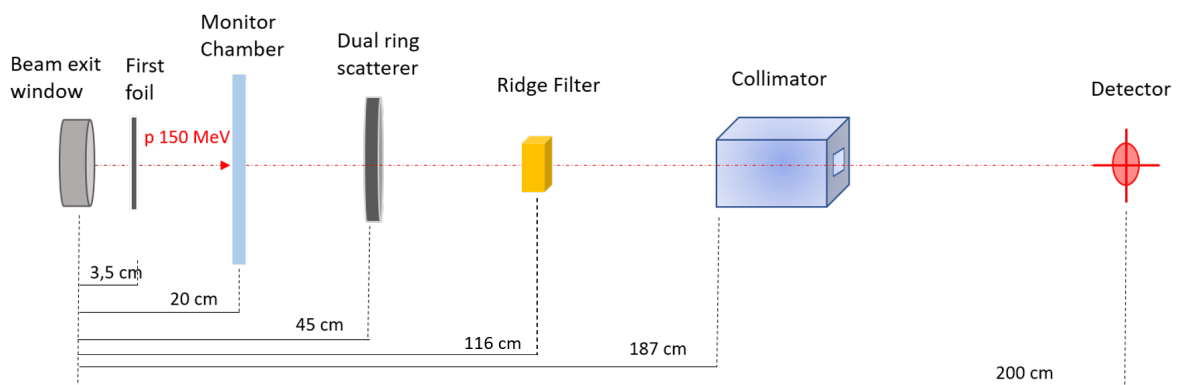


Figure 3.2: Schematic view of the setup of the dual ring passive scattering system at the HPTC bunker (not to scale), indicating the distances between beam exit window and the elements. The 150 MeV beam leaves the exit window and traverses the first foil, monitor chamber, dual ring scatterer, ridge filter, collimator, and finally reaches the detector or target.

The passive scattering system implementation used in the facility is inspired by the design proposed by Takada [44]. The proton beam first passes through the vacuum exit window behind which the first scatter foil is placed. This single lead foil produces the initial lateral beam spread. A beam ionization chamber monitor (BM1) is placed at 20 cm from the exit window in order to monitor the number of protons delivered. Then, the beam traverses the dual ring scatterer, placed at 45 cm from the exit window, which further broadens the beam. The spreading of the mono-energetic beam in energy is achieved by means of a range modulator. The HPTC experimental beamline implements a ridge filter designed and produced by GSI, Darmstadt [50], placed at 116 cm from the exit window. Finally, a collimator with a $5 \times 5 \text{ cm}^2$ squared aperture is placed upstream the other elements to conform the radiation field to the target in the lateral direction. The final beamline setup is composed by a pre-collimator made of PMMA (low-Z) with a thickness of 25 cm, and a Brass collimator (high-Z) with a thickness of 70 cm. A picture of the passive scattering beamline implemented in the HPTC is shown in Figure 3.3.

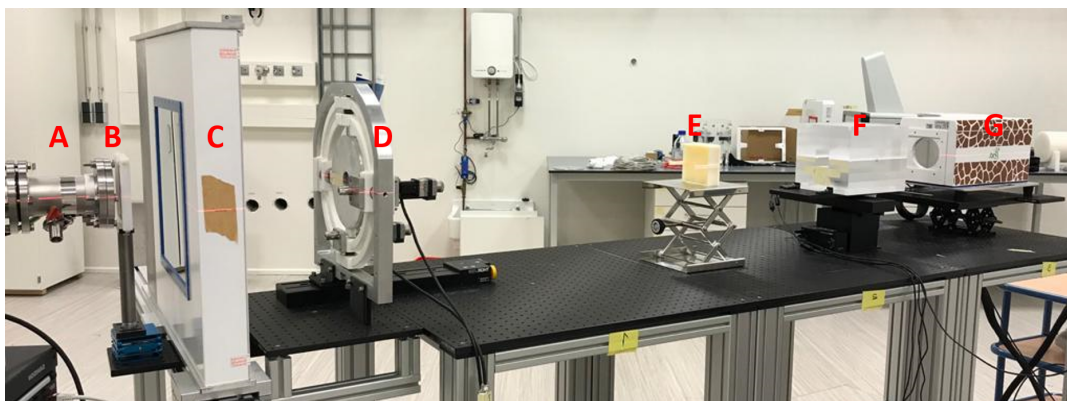


Figure 3.3: Complete passive scattering setup in the experimental room. The proton beam leaves the exit window (A) and goes through the first foil (B), monitor chamber (C), dual ring (D), ridge filter (E), collimator (F) and finally reaches the target (G).

To guarantee that a flat profile could be achieved in the target region, the first foil and dual ring needed to be optimized in terms of material composition, thickness, and dimensions. There is a trade-off to consider: a thicker scattering system will provide a larger field but it will reduce beam fluence, and vice versa. This work employed the scattering elements optimized by Tommasino et al. [47], as specified in Table 3.1. This characteristics are optimized to generate fields in the range $4 \times 4 \text{ cm}^2$ to $20 \times 20 \text{ cm}^2$. Moreover, as there is an interface between the two composing elements, achieving a proper beam alignment with the dual ring was key to guarantee a flat target distribution.

Table 3.1: Size and material of the scattering elements (first foil and dual ring) composing the setup used throughout this work.

First Foil		Inner Ring			Outer Ring		
Material	Thickness (mm)	Material	Thickness (mm)	Diameter (mm)	Material	Thickness (mm)	Diameter (mm)
Pb	3,4	Pb	5	50	Al	16	200

The optimal thicknesses of the PMMA pre-collimator and brass collimator used in the setup were found by means of MC simulations. PMMA and brass simulated blocks of different thicknesses were irradiated with a 150 MeV proton beam until we found a sufficient thickness that stops all the protons.

3.2.2. Detectors

In order to characterize the large fields in terms of field uniformity, lateral profile and depth dose distribution different types of detectors were used. This section provides a brief description of the detectors used during the experimental work. Moreover, these detectors output raw files that need to be processed. A MATLAB (version R2017a) script was written for each of the detectors to access the measurements, process their information and plot the outcomes.

Lynx 2D

The Lynx 2D detector [20] is a scintillating screen coupled to a CCD-camera. Its active surface area is of $30 \times 30 \text{ cm}^2$ with a 0.5 mm resolution. The incoming particles lose energy when traversing its gadolinium-based plastic material screen that is converted to photons via ionization. The CCD camera contains photodiodes that collect this light. This detector outputs beam lateral profiles in air, introduced in Section 2.2.2.

Giraffe

The Giraffe detector [19] is a high-resolution multi-layer ionization chamber used for measuring depth-dose curves in a single beam delivery. It has a circular aperture window of 12 cm of diameter and is composed of 180 layers, with a nominal range accuracy of around 0.5 mm. The output of the system is directly converted to a water-equivalent measurement.

MatriXX PT

The MatriXX PT detector [21], a quality assurance clinical device, is a 2d squared array comprising 1020 cylindrical ionization chambers. It outputs lateral profiles of the RBE dose in Gray. Following Section 1.2, these values need to be converted to physical dose by dividing by 1.1, i.e. protons RBE. The spacing between the chambers is 0.76 cm and its active area is $24.4 \times 24.4 \text{ cm}^2$. The dose measurement accuracy is of $\sim 1\%$ and a $\sim 1 \text{ mm}$ resolution when we implement bilinear interpolation [45]. The detector has a 0,64 cm WET build-up material on top of the detecting array.

3.2.3. Passive Field Characterization

The characteristics of the fixed single pencil beam of the experimental room in HPTC, in terms of beam shape, fluence and energy, were acquired as part of another master thesis project (A. Ibrahimi, personal communication, March 15, 2020). Once these properties were known, the fields produced by the passive scattering system needed to be characterized. This was achieved by measuring and analyzing the lateral beam profiles and their uniformity, the depth-dose distributions, and the relative dose at target position. For this purpose, we employed the detectors described in Section 3.2.2 and processed their outputs using MATLAB. The focus was on fields generated by mono-energetic proton beams with an initial energy of 150 MeV.

Lateral beam profiles and uniformity

The position and alignment of the elements in the beamline determine the characteristics of the radiated field. To achieve a field with an appropriate size and uniformity, the lateral beam profiles were analyzed. The beam-shaping elements were placed in the beam path in an initial position inspired by the work of the Trento Protontherapy center [47]. Then, their distances from the exit window were optimized by analyzing the profiles' uniformity, measured using the Lynx 2D detector.

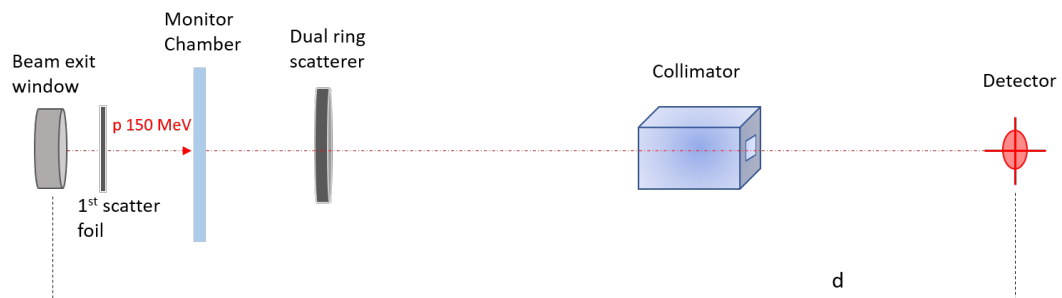


Figure 3.4: Schematic view of the dual ring passive scattering setup, excluding the ridge filter. The 150 MeV beam leaves the exit window and traverses the first foil, monitor chamber, dual ring scatterer, ridge filter, collimator, and finally reaches the detector or target.

First, the appropriate positions of the dual ring and detector were found using a setup that did not include the collimator. In this setup, the proton beam passes through the vacuum exit window where the first scatter foil is placed. A beam ionization chamber monitor (BM1) is fixed at 20 cm from exit window. Then, the dual ring scatterer is mounted on a motorized support which allows to precisely align the ring with respect to the beam in any direction, including forwards and backwards, as a function of the measured lateral profiles uniformity. The detector can also be displaced. Second, the PMMA collimator was added to the setup (Figure 3.4) and the uniformity checks were performed for different positions.

The Lynx detector provides raw outputs that can be extracted as .csv files. These were processed using a MATLAB script. First, the values were imported using the `readtable` function and converted into a matrix of values using the `table2array` function. The resolution of the Lynx detector is 0.5 mm, so this step resulted in a 600×600 grid. In order to find the beam profile and its corresponding uniformity, we integrated over the rows (x-profile) and over the columns (y-profile), and then we studied the uniformity over a region of interest. The uniformity was evaluated by checking the maximum (I_{max}) and minimum (I_{min}) values in terms of signal intensity:

$$U[\%] = 100 \left(1 - \frac{I_{max} - I_{min}}{I_{max} + I_{min}} \right) \quad (3.1)$$

This approach is widely used in literature (see Section 2.2.2). We extracted the uniformity of different field sizes by changing the region in which we search for the I_{max} and I_{min} . Then, we plotted the x-y lateral pro-

files, normalizing them to the center value. Moreover, the 2d-dose distributions show the matrix of dose values captured by the detecting surface.

Depth-dose distributions

Depth-dose curves were obtained with the purpose of establishing the range-energy relationship of the system and to obtain data to benchmark the MC model. We measured the Bragg curves both in air and with beam-shaping elements in the beamline.

The depth-dose distributions in air were first evaluated using the commissioning data of the research beamline provided by Varian. These measurements were acquired on a water tank placed at the beam isocenter, i.e. 91,1 cm, as shown in Figure 3.5, following the procedure specified in Section 2.2.1. The Bragg curves

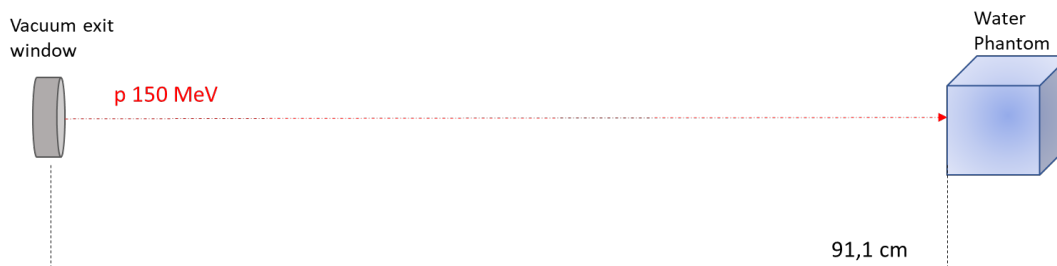


Figure 3.5: Schematic view of the water phantom setup used to measure pristine Bragg curves in air. The 150 MeV proton beam leaves the exit window and traverses air until it reaches the water phantom, placed at isocenter.

were then measured using the Giraffe detector. The detector was placed 200 cm away from the exit window, aligned to the beam using the bunker laser system. Three different measurements were taken using the setup in Figure 3.2 with slight modifications: **a)** pristine Bragg peak curves in air, **b)** pristine Bragg curves with all beamline elements in place, and **c)** SOBP curves with the ridge filter in place as well.

The .csv raw outputs of the Giraffe detector were directly read and plotted using a MATLAB script. The Bragg curves were then normalized to the maximum value. The uniformity of the SOBP width was computed using Equation 3.1, with I_{max} and I_{min} replaced by the maximum and minimum dose values. These values were obtained in a region of interest that was chosen manually, which allowed to compute the uniformity for different modulation widths.

Relative dose measurements

The dose deposited in the target needs to be known for most radiobiological applications. Furthermore, field flatness, i.e. uniformity, and symmetry are a demand to ensure the target is irradiated homogeneously and with known properties. The goal of these experiments was to measure the dose of the field using the passive scattering setup (Figure 3.4), with no ridge filter in place, and to further verify its uniformity. The experiments were performed using the MatriXX PT detector, and for two different collimating elements: **a)** a PMMA collimator alone, and **b)** a PMMA pre-collimator and a Brass collimator. Throughout these experiments, the MatriXX PT detector was positioned 200 cm away from the exit window. To capture the delivered dose at different Bragg curve position (plateau and peak), RW3 water equivalent plates were placed in front of the MatriXX.

The MatriXX detector provides raw .csv files that are processed using a MATLAB script, following a similar procedure to the one described for lateral beam profile files obtained using the Lynx detector. After reading the values from the files and converting them into a matrix of dose values, we performed bilinear interpolation using *interp2*. This way, we improved the resolution from 3,8 mm to ~ 1 mm, as recommended in literature [9].

The x and y-profiles were obtained and represented in the same way as for the lateral beam profiles measured with the Lynx detector. Moreover, equation 3.1 was used to evaluate the uniformity, where I_{max} and I_{min} are the maximum and minimum dose values over the region of interest.

3.3. TOPAS Simulations

The passive scattering system model designed using TOPAS starts at the nozzle exit. The aims of having reliable MC simulations are to evaluate and optimize the beamline elements, to allow the verification of the beamline design using a computational method and to assist with the preparation of the system setup for radiobiological experiments [18]. For having a trustworthy model, both the pencil beam and the complete passive scattering beamline were benchmarked with experimental data. The TOPAS output files were analyzed using MATLAB.

3.3.1. Simulation settings

The simulation of the passive scattering beamline was performed using the TOPAS code. The details on this code are specified in Section 1.5. There are five elements to consider for modeling the beamline: the physics settings, the geometry description, the beam source description, the scoring and the uncertainty of the simulations.

Physics settings

The “TOPAS default modular physics list” was used in all the simulations. The interactions modeled are specified in Table 3.2. The production range cuts, i.e. limit at which a particle stops being tracked and deposits its energy locally [36], were kept to its default values. The maximum step size, i.e. maximum length that a particle traverses before a new calculation is done, was varied depending on the scorer to be at least one-fifth of the smallest feature of the voxel grid used as scorer (J. Brown, personal communication, January 17, 2020).

Table 3.2: TOPAS physics settings chosen for the passive scattering model. Each module specifies a type of simulated interaction.

Module Name	Simulated Interactions
g4em-standard_opt4	Electromagnetic interactions
g4h-phy_QGSP_BIC_HP	Nuclear interactions using binary cascade model
g4decay	Decay of excited residual nuclei
g4ion-binarycascade	Nuclear interactions of light ions using binary cascade model
g4h-elastic_HP	Elastic scattering
g4stopping	Capture of charged particles at rest

Geometry description and scoring elements

The beamline elements were modeled to reproduce the ones in Figure 3.3. The scattering system and collimators were modeled down to millimeter accuracy following the manufacturer’s blueprints. Moreover, the beam monitor chamber (BM1) was implemented in the simulation to consider the energy loss and the slight lateral spread caused by it. It was modelled as a water slab with its water equivalent thickness (WET). The WET was obtained experimentally by measuring the depth-dose curves with and without the monitor chamber and computing the difference in range.

The goal of the scoring elements is to obtain the simulated depth-dose distributions and lateral beam profiles, at different positions along the beamline. These scorers were modeled as a simplification of the detectors described in Section 3.2.2. No underlying physics was implemented:

- The lateral intensity profiles were scored reproducing the Lynx detector. The scorer is an air slab, of arbitrarily 2 mm, with a $30 \times 30 \text{ cm}^2$ resolution in the plane perpendicular to the beam. Depending on the number of voxels in which this volume is divided, the resolution varies. This scorer tallies the number of particles arriving to its surface area.
- The lateral dose profiles were simulated using a scorer that reproduces the MatriXX PT. The scorer is a planar water slab of the same dimensions as the detector in the x-y plane, with 1 mm thickness. The scoring volume is divided in voxels, and each of them collects the total dose deposited in it. The number of voxels can be modified to keep a balance between the resolution of the scorer and the statistical accuracy. A water block of 0.64 cm was placed prior to the scoring volume to account for the thickness of the build-up material of the detector.
- The depth-dose distributions were simulated to mimic the Giraffe detector. The Giraffe outputs its values as water-equivalent measurements; therefore, the scorer is designed as a water cylinder of the

same diameter as the detector, i.e. 10 cm, divided in several slabs along the depth axis. The number of slabs is chosen to obtain a good spatial resolution while maintaining appropriate statistics. This score tallies the dose deposited in the medium in each slab.

Beam source description

As the literature study concluded (Chapter 2), the pencil beam at the exit window needs to be parametrized using four beam parameters: lateral spread, angular spread, energy spread and mean energy. These values were obtained by comparing the beam envelope and pencil beam depth-dose curves measurements and simulations (Section 3.3.3) and tuning the beam source parameters until agreement was found among them.

3.3.2. Data analysis and statistical uncertainty

The output of the scored quantities resulting from the TOPAS simulations are .csv files. These files are read and processed using MATLAB (version R2017b), following different approaches depending on the scoring element.

The data extracted from the MC simulations has statistical uncertainty. TOPAS allows reporting as an output of the simulation the standard deviation (σ) linked to the distribution of the quantity of interest [35]. Instead of using batches to compute σ , they use the history by history method. A description of this method is out of the scope of this project. The uncertainty is then computed, following the approach described in the TOPAS documentation [26], as $\sigma * \sqrt{N}$, where N corresponds to the number of histories that produced that distribution. If the scorer is a surface or volume divided in many voxels, each voxel has its corresponding uncertainty.

3.3.3. Validation of the pencil beam

MC models of passive scattering systems start at the nozzle entrance (see Section 2.1.2). Therefore, the information about the pencil beam at this point is required. The four parameters defining the beam source characteristics are mean energy, energy spread, angular spread, and lateral spread. To obtain these, we needed to simulate the pencil beam and compare the outcomes with experimental data: beam envelope and depth-dose distributions. These data were provided by another master thesis project (A. Ibrahim, personal communication, March 15, 2020) and served as the first benchmark of the MC simulation. The main focus of this project is on a 150 MeV mono-energetic proton beam.

Beam envelope simulations

The beam envelope is the evolution of the transversal profile of the beam in air as a function of the distance from the exit window. It is used to measure spot profiles at various distances from the exit window. The beam envelope was simulated to reproduce the experimental beam envelope in order to obtain the initial parameters of the beam source placed at the exit window, specifically the lateral spread and angular spread.

The beam envelope experiment consisted of seven spot measurements, acquired one by one at seven different distances from the exit window, using the Lynx detector. These distances were: 23 cm, 53 cm, 91,1 cm, 123 cm, 153 cm, 183 cm and 204,5 cm. The position at 91.1 cm corresponds to the beam isocenter. The analysis of the experimental results, presented later in the figures of this report, is part of another master thesis project (A. Ibrahim, personal communication, March 15, 2020).

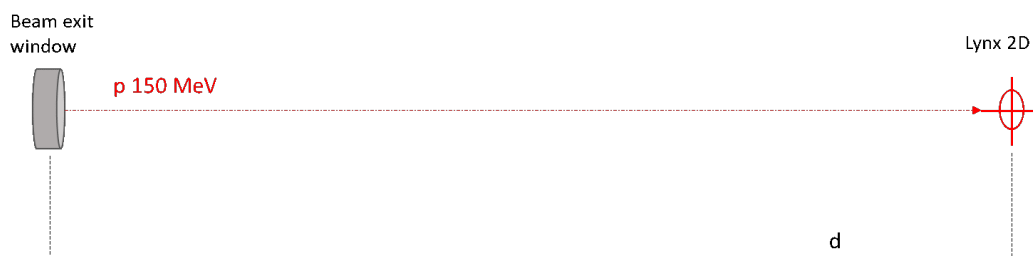


Figure 3.6: Schematic view of the setup used to measure the beam envelope. The 150 MeV beam leaves the exit window and traverses air until it reaches the Lynx detector.

The beam envelope was simulated for three different energies: 70, 150 and 240 MeV. The mean energy used

as input for the beam envelope simulations was the energy at the exit window for each given nominal energy, reported by the beam commissioning measurements.

The simulation setup reproduces the experimental one, presented in Figure 3.6: seven slabs of 30x30 cm² each, representing the dimension of the Lynx detecting surface placed along the beam path in air at the same distances as in the experiment. The only element included in the beamline simulation is the Kapton of the vacuum exit window. The TOPAS scoring surface is a slab divided in a number of voxels in the transversal plane which guarantees both a good spatial resolution and appropriate statistics.

Each of the seven positions was analyzed separately in MATLAB. The .csv TOPAS output files providing the number of particles arriving to each voxel were read using the *importfile* function and then converted into a matrix that reproduces the scoring surface. The horizontal and vertical central profiles, perpendicular to the beam direction, were extracted from the matrix central row and column, respectively. Each of these profiles was fit using the *fit* function, which implements the following Gaussian function:

$$f(x, \mu, \sigma) = \frac{1}{\sqrt{2\pi}\sigma} e^{-\frac{(x-\mu)^2}{2\sigma^2}} \quad (3.2)$$

Where μ is the center value and σ is the standard deviation of the Gaussian. This fitting can be done because the beam spot profiles measured have a Gaussian shape. The standard deviation of the beam profile simulated at each of the seven positions, as well as its error, are provided by the Gaussian fit. The standard deviation therefore represents the beam width in the x and y profiles. However, it cannot be assumed that the simulation output is of equal quality voxel-by-voxel. To overcome this, a weight factor ($\frac{1}{\text{uncertainty}}$ of each voxel) was added to the *fit* function to determine how much each voxel value influences the final fit. This way, those scores with a lower standard deviation have a higher influence than those with a higher one.

Depth-dose distributions

The simulation of depth-dose distributions is used to obtain beam source parameter values, i.e. mean energy and energy spread, and to benchmark the MC model.

First, the depth-dose distributions in air were simulated reproducing the water phantom setup (Figure 3.5). The simulation setup includes a water block placed after the exit window and a 30 x 30 x 30 cm³ water volume. The water block has the thickness corresponding to the sum of the WET of all elements placed in the beamline, i.e. water tank PMMA wall, Markus Chamber, Kapton window, air. The reason for this simplification is the high complexity and lack of specifications for all these elements. This approach is similar to the one described by Beltran et al. [6], in which the authors condense all the beamline elements of their passive scattering system into a single lead foil.

Second, the depth-dose distributions were simulated using a MC setup that only includes the detecting volume, which reproduces the Giraffe detector, the Kapton at the exit window, and a water block that has the WET of the BM1.

In both cases, the .csv TOPAS output files provided a list with the values of the dose deposited in each of the slabs in which the detecting volume is divided, in the depth direction. These files were processed using MATLAB and imported using the *importfile* function. The curves were normalized to their maximum value, corresponding to the Bragg peak. To obtain the *d*20 and *d*80 values, a linear interpolation of the Bragg curve data points using the *interp1* function was performed.

3.3.4. Passive scattering simulations

Once the pencil beam simulations were benchmarked and the beam source parameters were estimated, we simulated the lateral field profiles, the Bragg curves, and the dose distributions for a 150 MeV mono-energetic proton beam using our TOPAS model of the passive scattering system. This data was later used to benchmark the model by comparing it with the experimental data acquired in Section 3.2.3.

Lateral field profiles

The MC simulation of 2D distributions and lateral profiles is done to benchmark the TOPAS model of the passive scattering beamline against measurements. This way, both the TOPAS physics model and beamline

elements design can be validated.

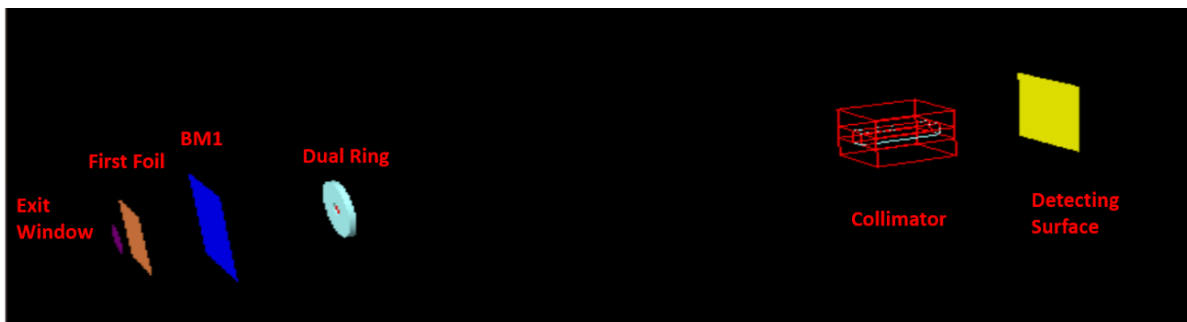


Figure 3.7: Geometry of the passive scattering system implemented in TOPAS, including the exit window, first foil, BM1 (monitor chamber), dual scattering ring, PMMA collimator and the scoring surface.

Following the same approach as for the experimental measurements described in Section 3.2.3, lateral field profiles were computed for two passive scattering system setups: one in which the beam traverses the exit window, first foil, BM1 and dual ring alone; another one in which the beam is also laterally conformed by the presence of the PMMA collimator (Figure 3.7). The latter reproduces the experimental setup presented in Figure 3.4.

The scorer is a planar surface divided in 150x150 voxels; thus, its resolution is of 2 mm. This is lower than the original Lynx resolution of 0.5 mm. Therefore, each of the 22500 voxels receive a score for the measured physical quantity. The decrease in resolution is done to improve the simulation statistics without excessively increasing the computational and time expenses. This is acceptable because large field irradiation are in the order of centimeters.

This work compares two different approaches for processing the simulated lateral profiles using MATLAB. The first method consists in directly extracting the lateral x and y profiles from the scoring grid, following the procedure described in Section 3.2.3 for the experimental lateral beam profiles. The second one uses radial projection to reduce the statistical uncertainty of lateral profiles generated by MC simulation with a limited number of simulated primary protons. This approach outputs an approximation of the actual lateral profiles because the method is based on the assumption that the beam is axis-symmetric.

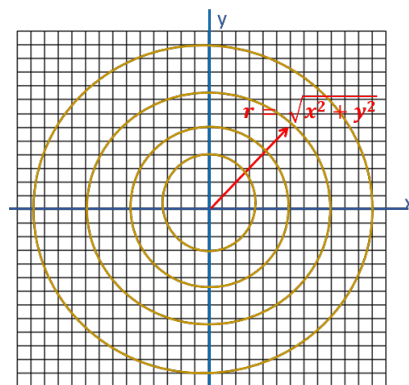


Figure 3.8: Projection of voxels on a square grid to a one-dimensional axis by dividing it in rings and computing the radial distance of each voxel to the center of the grid.

The process followed to implement the radial projection method is as follows:

1. Convert the raw TOPAS file into a matrix. Each position of the matrix corresponds to the score measured at each voxel in which the detecting surface is divided. The first method shares this step.
2. Create a grid of the same dimensions as the voxel grid, e.g. 150 x 150, where each pixel contains the distance of each voxel from the original grid to the grid centre (x_0, y_0) , i.e. its radius. This distance is

computed as follows:

$$r r_i = \sqrt{(x_i - x_0)^2 + (y_i - y_0)^2} \quad (3.3)$$

Where i refers to a given voxel of the original square grid.

3. Choose the number of rings in which the voxel grid will be divided, e.g. 75 rings. The distance among subsequent rings is always the same. Steps 2 and 3 are depicted in Figure 3.8.
4. Create an array of the same length as the number of rings. Then, define an inclusion criterion which determines which voxels are included in a given ring based on their distance to the center: if radius of the inner ring $< r r_i \leq$ radius of the outer ring, $r r_i$ pertains to that ring.
5. Sum all the voxel scores contained in a ring and input that value into the array, e.g. the first array position will contain the sum of the scores of all the voxels located inside the first ring. Normalize by dividing by the number of voxels contained in that ring. This is similar to performing a normalization by area but overcoming the limitation of having a relatively large voxel size.

The output of using this approach is an array of a length defined by the number of rings. Each value corresponds to the sum of all detected scores by the voxels in that region, normalized by the number of voxels per ring. Ding et al [10] proposed a similar method for processing pencil beam lateral profiles.

Once the lateral beam profiles were extracted from the simulation, the uniformity was computed using Equation 3.1. Moreover, since each voxel score has a standard error linked to it, the statistical uncertainty of each ring was computed in parallel by following the same radial projection method. Each score was given the same weight; therefore, the error over a region of interest was computed as the average error of all the values corresponding to each region.

Depth-dose distributions

Depth-dose distributions were simulated, and the raw outputs were processed, following the same procedure as described in Section 3.3.3. To do this, we used a MC model that reproduces the setup in Figure 3.2, which employs the Giraffe detector. First, the pristine Bragg curves were simulated by removing the ridge filter from the model (Figure 3.4). Second, we simulated the SOBPs having all the beamline elements in place (Figure 3.3).

Dose distributions

MC dose simulations are used to estimate the irradiation time required to deposit a given dose in a specific target, the location of the Bragg peak and the dose uniformity. Having a benchmarked passive scattering model can therefore be used to assist in the preparation of radiobiological experiments which require different doses and setups. To perform these simulations, we employed the MC model depicted in Figure 3.7. The simulated dose was deposited in a detecting surface that reproduced the MatriXX detector (section 3.2.2).

As first, the ratio between the simulated target dose and the number of primary protons measured allow to make a guess of the primary protons required to obtain a given dose in the target. Using MATLAB, we computed the total dose in the target area by summing the dose deposited at each voxel. Previous measurements performed in another master thesis project (A. Ibrahim, personal communication, March 15, 2020) show that the proton current for a 1 nA beam extraction current is of around 2×10^7 p/s for a 150 MeV beam. Using this knowledge, we correlated the fluence of the particles (p/s) with the simulated dose arriving at the target surface.

In the next step, we employed the MC simulations to estimate the location of the Bragg peak. To achieve so, water slabs were placed before the detecting volume and we compared the mean dose deposition in the target area with the experimental results. The thickness of this water volume therefore determined which point of the Bragg curve we were measuring.

At the end, we benchmarked the simulated lateral beam dose profiles using the experimental data data acquired using the procedures described in Section 3.2.3 to further validate the physics and beamline models. To achieve this, the radial projection approach described in the previous section was used to generate the profiles and their uniformity was computed using Equation 3.1.

4

Results and Discussion

In this chapter, the results and discussion are presented. First, the comparison between the pencil beam data and the simulation is shown. The results of this comparison have been used to find the beam source parameters used as input of the MC model created using TOPAS. Afterwards, the experimental results of the passive beam experiments are presented. Moreover, those data have been compared with the MC simulations to benchmark the model.

4.1. Validation of the Pencil Beam

Benchmarking the pencil beam simulations with experimental data provides an estimation of the beam source parameters, used as input of the passive scattering MC model. For this purpose, we compared the simulated beam envelope with the experimental one to obtain an estimation of the lateral and angular spread, following the approach described in Section 3.3.3. Moreover, we measured and simulated pristine Bragg curves in air, from which we acquired the initial mean energy and energy spread values for the pencil beam.

Beam envelope

The beam envelope was simulated in air by reproducing the experimental setup presented in Figure 3.6. Seven air slabs were simulated along the beamline to obtain the central profiles (Figure 4.1). The TOPAS scorer is a plane divided in a number of voxels which ensures both good statistics and resolution.

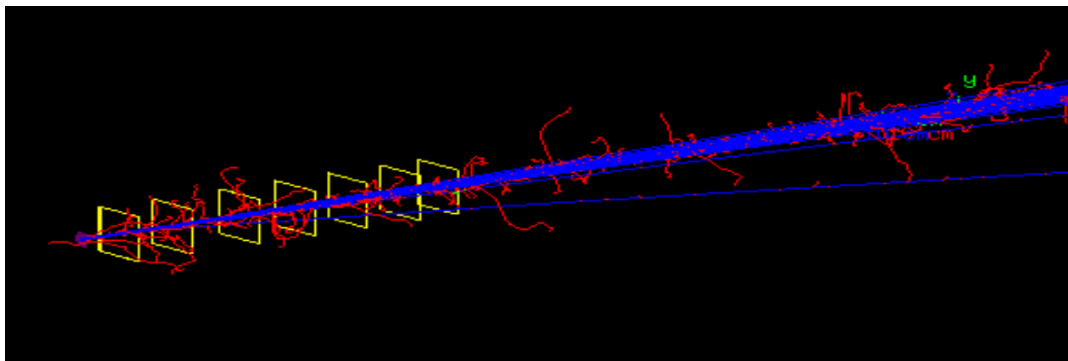


Figure 4.1: TOPAS visualization of the geometry implemented to perform the beam envelope measurements. The beam traverses seven air slabs (placed at 23 cm, 53 cm, 91,1 cm (isocenter), 123 cm, 153 cm, 183 cm and 204,5 cm) each of them being a scoring grid.

Figure 4.2 shows the agreement between the central profiles, which are Gaussian, for a 150 MeV proton beam, for both experimental and simulated data, computed at isocenter position, i.e. 91,1 cm. The central profiles were then analyzed to extract the beam envelope for three beam energies (70 MeV, 150 MeV and 240 MeV), following the procedure described in 3.3.3. For a nominal energy of 150 MeV, Figure 4.3 shows the simulated beam envelope in x and y direction, and Figure 4.4 presents the comparison of the beam envelope, for both measurements and simulations in x and y direction. 10^7 primary protons were simulated to obtain these

figures to ensure good statistics. The simulated envelope is within the error bars of the measured one. The beam envelope shows the divergent beam optic settings of the transport beam line. The beam focus is, in fact, before the vacuum exit window. The first points before isocenter still show a slight effect of the ion optics settings together with the multiple Coulomb scattering in air, while after isocenter the main contribution is given by the multiple Coulomb scattering.

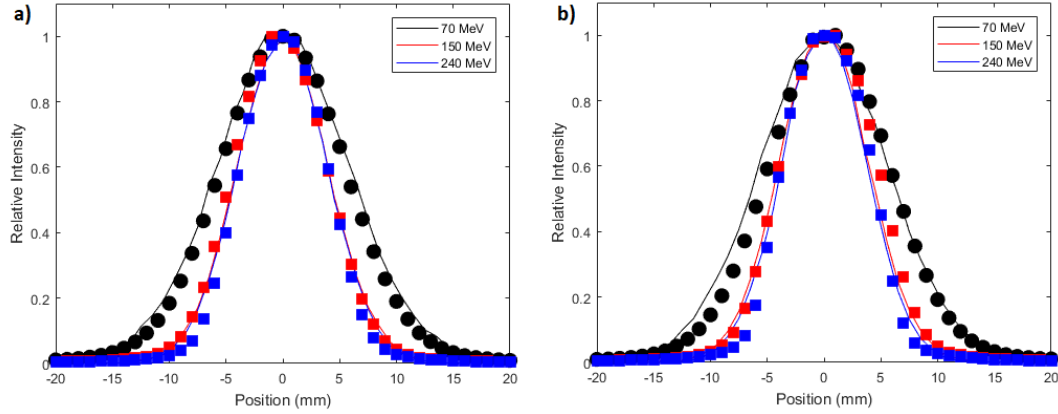


Figure 4.2: Beam spot profiles of 70, 150 and 240 MeV measured and simulated at the isocenter position (91,1 cm) (a) x-profile, (b) y-profile. The simulated data is presented as lines. The experimental data (solid points), were acquired from another master thesis project (A. Ibrahim, personal communication, March 15, 2020). 10^7 primary protons were simulated for each energy.

In order to reproduce the experimental data in terms of spot shape and size, a tuning of the initial angular and lateral spread, used as beam source input parameters, was performed by running multiple beam envelope simulations and comparing them with the experimental ones. These parameters highly influence the beam lateral spread after traversing all the beamline elements (see Sections 2.1.2 and 2.2.2). Table 4.1 summarizes the parameters values for which the agreement was found, for the three different energies. Those values are used as a starting point for the subsequent simulations. Moreover, to obtain these results, we initially employed Varian's estimates of the mean energy and energy spread. Then, we used the parameters acquired in the following section (Table 4.4) and verified that changes in initial energy and energy spread do not influence the beam envelope agreement.

The difference in lateral spread in x and y direction presented in table 4.1 reflects the asymmetry of the beam. Also, the beam suffers a slightly higher divergence in the vertical direction which is reflected in the higher y-direction angular spread value. These two effects are showcased in the simulated beam envelope in Figure 4.3 for the x-y profiles. By comparing the different energies in the table, it is possible to observe that the higher the energy, the smaller the spot size. This is due to the materials located in the energy selection system implemented after the cyclotron.

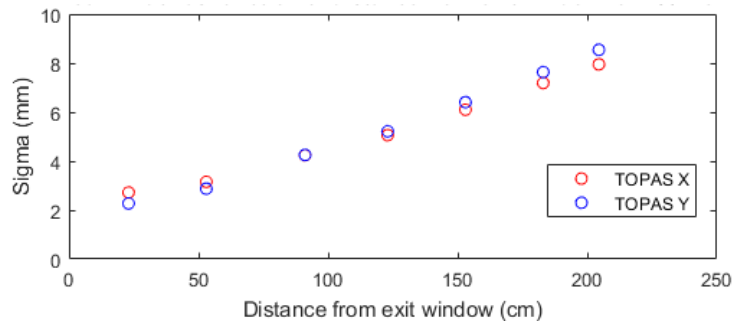


Figure 4.3: Beam envelope simulated for 150 MeV. The Gaussian standard deviations derive from a fit of the X (horizontal) and Y (vertical) central profiles of the spot distribution, as a function of the distance from the exit window. The simulation scoring grid is divided into 1200x1200 voxels. The simulation uncertainty comes from the statistical Gaussian fit error and the scorer resolution. 10^7 primary protons were simulated for each direction.

Table 4.1: Initial beam source parameters (lateral spread and angular spread) for 70 MeV, 150 MeV and 240 MeV.

Nominal Energy (MeV)	Lateral spread (x) (cm)	Lateral spread (y) (cm)	Angular spread (x) (rad)	Angular spread (y) (rad)
70	0,33	0,25	0,0038	0,0042
150	0,275	0,21	0,00275	0,0032
240	0,245	0,18	0,0032	0,0034

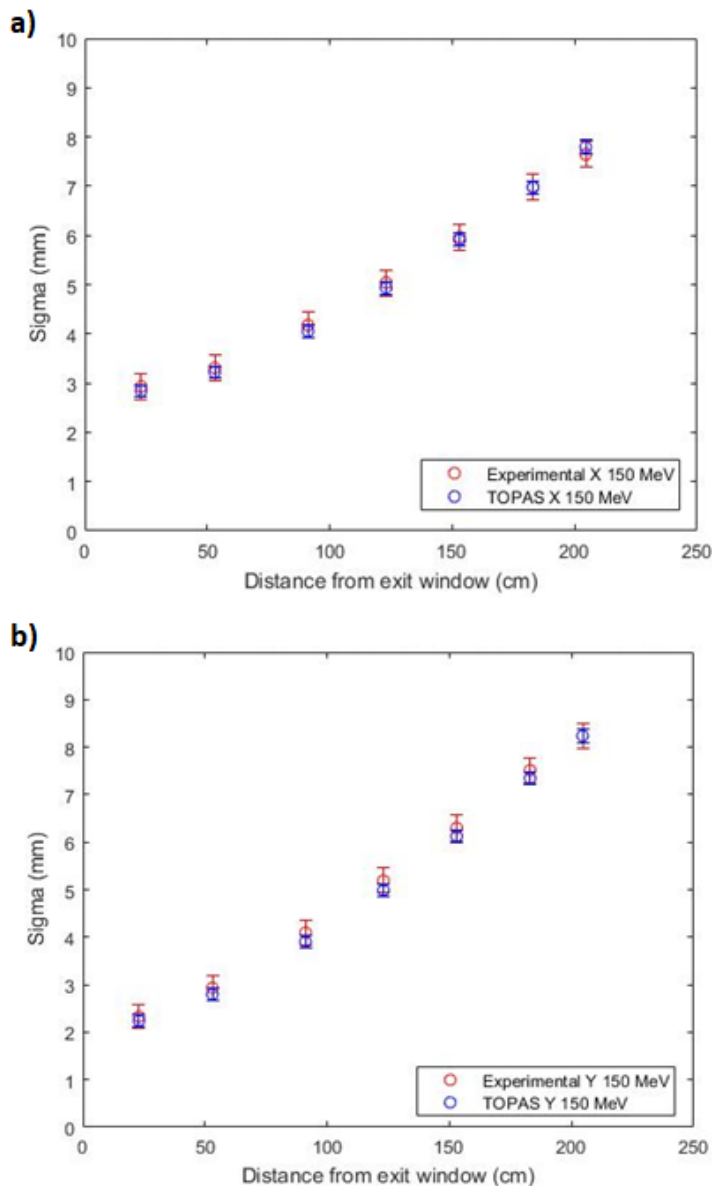


Figure 4.4: Beam envelope measured and simulated for 150 MeV. The Gaussian standard deviations derive from a fit of the a) X (horizontal) and b) Y (vertical) central profiles of the spot distribution, as a function of the distance from the exit window. The simulation scoring grid is divided into 1200x1200 voxels. The simulation uncertainty comes from the statistical Gaussian fit error and the scorer resolution. The experimental data was provided from another master thesis (A. Ibrahim, personal communication, March 15, 2020). 10^7 primary protons were simulated for each direction.

Depth-dose distributions

This section evaluates the agreement between the experimental and simulated depth-dose distributions in air. Sections 3.2.3 and 3.3.3 describe the two sets of experimental and simulated data used and their corresponding setups, i.e. water phantom setup and Giraffe setup. The values were normalized to their maximum value, corresponding to the Bragg peak. The d_{20} and d_{80} were obtained by performing a linear interpolation

of the distal fall off, for both experimental and simulated data.

The choice of the number of simulated primary protons is based on the trade-off between computational expense and statistical uncertainty. Figure 4.13 shows that for 10^7 histories, which was our choice, the statistical uncertainty in the plateau and Bragg peak is under 2%. The fall-off region has a higher uncertainty because a lower number of particles is scored in that region.

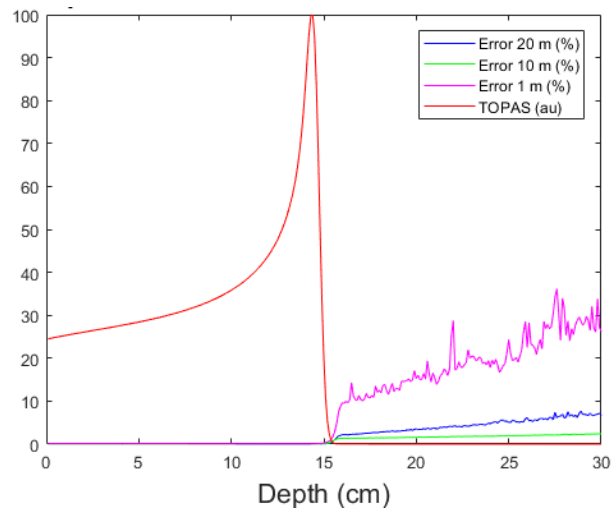


Figure 4.5: Comparison of the statistical uncertainty (%) of a relative depth-dose curve (in red, for reference) simulated with a different number of primary protons (Blue: 20 million, Green: 10 million, Pink: 1 million). The Y-axis values correspond to % error and % relative dose.

To match the simulated depth-dose curves to the experimental ones, we followed the most common approach found in literature, described in Section 2.1.2. It consists of performing various simulations only modifying the initial energy and the energy spread of the beam, until optimal agreement is reached. Thus, we could determine that the initial beam energy and energy spread employed for the TOPAS simulation are consistent with the real ones. Figure 4.6 shows the effect that having different energy spread for the same energy has on the Bragg peak width and on the peak-to-plateau ratio.

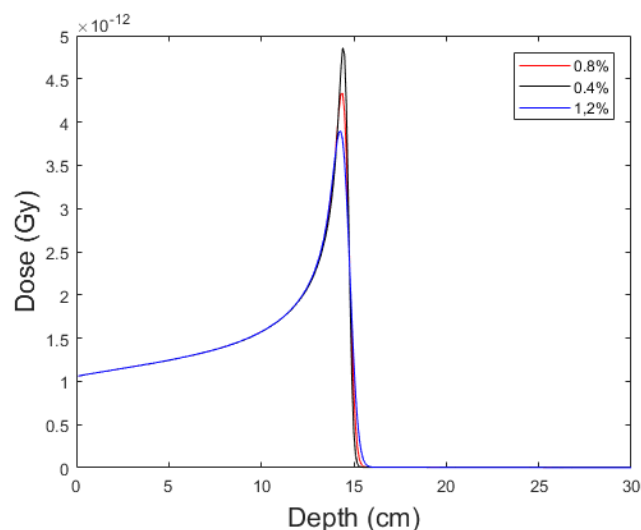


Figure 4.6: Simulated pristine Bragg curves in air for a mono-energetic 150 MeV beam with an energy spread of 0,8% (red), 0,4% (green), 1,2% (blue). Simulation for 10^7 proton histories.

Figure 4.7 shows the comparison between experimental and simulated depth-dose distributions using the setup in Figure 3.5 (water phantom depth-dose distribution data for a nominal energy of 150 MeV). Both

curves are normalized to the maximum value. The beam parameters for which the best agreement was found are presented in Table 4.2. The table also includes the distal fall-off ($d20 - d80$) and range values ($d80$) for both the simulation and measurements. The TOPAS simulations matched the experimental data for a simulated beam energy of 149.9 MeV and energy spread of 0.8%. The entrance channel and the distal fall-off show a good agreement with a difference in the proton range of 0.3 mm. Furthermore, Table 4.2 shows the effect of modifying the mean ionization potential of water from the Geant4 default value (78 eV) to other accepted values in literature (75 eV). This was discussed in Section 1.1.1. The uncertainty in the energy loss becomes apparent in the range shift of 5 mm.

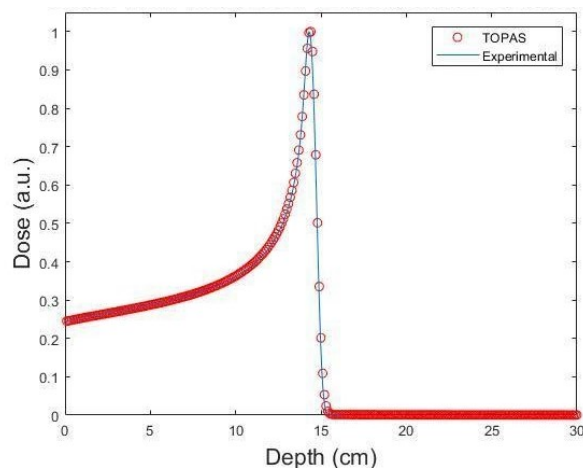


Figure 4.7: Experimental (blue) pristine Bragg curve for 150 MeV proton beam (nominal energy) and simulated pristine Bragg curve using the water phantom setup. The simulation input parameters are: initial energy 149,9 MeV, energy spread 0,8%, and lateral and angular spread as specified in table 4.1. Simulation for 10^7 proton histories.

Table 4.2: Energy and energy spread used as input for the simulation to achieve agreement with measured $d20-d80$ (distal fall-off) and $d80$ (range) pristine Bragg curve values in air, for the water phantom setup, for a nominal energy of 150 MeV. Simulation for 10^7 proton histories using two mean ionization potential values for water. The uncertainty of the measurements and simulations is of 0,5 mm, given by the detecting volume resolution. The measurement values are courtesy of Varian.

	Initial Energy (MeV)	Energy Spread (%)	$d20-d80$ (cm)	$d80$ -range (cm)
Simulation (75 eV)	149,9	0,8	0,38	14,62
Simulation (78 eV)	149,9	0,8	0,38	15,09
Measurement	149,9	-	0,38	14,59

The agreement between simulated and measured Bragg curves was also found for three other energies: 70, 200 and 240 MeV. Table 4.3 summarizes the parameters which best reproduce the experimental data. We can observe a general trend concerning the energy spread: the higher the nominal energy, the lower the energy spread relative to the initial energy.

Table 4.3: Energy and energy spread used as input for the simulation to achieve agreement between measurements and simulations for pristine Bragg curve values in air, for the water phantom setup, for 4 different nominal energies (70 MeV, 150 MeV, 200 MeV, 240 MeV). Simulation for 10^7 proton histories.

Nominal Energy (MeV)	Initial Energy (MeV)	Energy Spread (%)
70	69,87	1,24
150	149,9	0,8
200	199,41	0,62
240	239,42	0,25

Figure 4.8 shows the comparison between experimental and simulated depth-dose profiles for the setup using the Giraffe detector. Both curves are normalized to the maximum value. The beam source parameters for which the best agreement with experimental data is found are summarized in Table 4.4, along with the

measurement values. The range and distal fall-off are also included. The TOPAS simulations matched the experimental data for a simulated beam energy of 150.2 MeV and energy spread of 0.85%. Both distal fall-off and range show agreement. However, the entrance channel shows slight disagreement probably given by an electron build-up effect which occurs in devices such as the Giraffe. The MC model does not simulate this effect because the materials of the Giraffe detector are not implemented. Experimentally it is possible to add a thin absorber to stop the electrons and avoid this effect. However, this correction was not made for this experimental data.

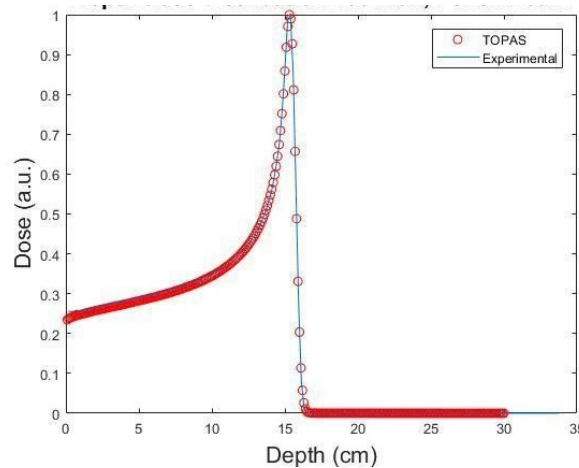


Figure 4.8: Experimental (blue) pristine Bragg curve for 150 MeV proton beam (nominal energy) and simulated pristine Bragg curve using the Giraffe setup. The simulation input parameters are: initial energy 150,2 MeV, energy spread 0,85%, and lateral and angular spread as specified in table 4.1. The uncertainty of the measurements and simulations is of 0,25 mm and 0,5 mm, respectively. Simulation for 10^7 proton histories.

Table 4.4: Energy and energy spread used as input for the simulation to achieve agreement with measured d20-d80 (distal fall-off) and d80 (range) pristine Bragg curve values in air, for Giraffe setup, for a nominal energy of 150 MeV. Simulation for 10^7 proton histories. The uncertainty of the measurements and simulations is of 0,25 mm and 0,5 mm, respectively, given by the detecting volume resolution.

	Initial Energy (MeV)	Energy Spread (%)	d20-d80 (cm)	d80-range (cm)
Simulation	150,2	0,85	0,39	15,61
Measurement	150,2		0,39	15,6

The measured value for the initial beam energy for the setup using the Giraffe, i.e. 150,2 MeV, was 0,3 MeV higher than for the water phantom setup, i.e. 149.9 MeV. This difference is below the 0,5 MeV experimental uncertainty of the beam. Furthermore, for the water phantom setup, the energy at the exit window is computed taking into account the WET of the elements the beam traverses. Taking these two uncertainties into account, we could expect both energy measurements at exit window to be in agreement. Moreover, as expected, the initial beam energy defined in both TOPAS simulations corresponds to the energy at exit window found experimentally.

By comparing the experimental measurements in Table 4.2 (water phantom) and Table 4.4 (Giraffe), it can be observed that the experimental range ($d80$) using the water phantom depth-dose distribution (14,59 cm) data is 1 cm lower than the one measured with the Giraffe detector (15,6 cm). This is related to the differences in experimental setup, described in Section 3.2.3. The water phantom setup includes multiple elements in the beamline: a water tank with a non-negligible wall and two ionization chambers. These elements cause energy loss, reducing the beam range. The WET of these three materials add up to 1,01 cm, which agrees with the expected range decrease. The Giraffe detector, on the other hand, outputs values that compensate for this energy loss, thus explaining the range difference among the two methods.

All in all, the initial mean energy and energy spread values for the 150 MeV pencil beam, presented in Table 4.4, are kept as the initial beam parameters to be used for subsequent simulations. These parameters are chosen rather than the ones in Table 4.2 because: **a)** the Giraffe measurements are more recent, **b)** less

elements in the beamline allow a more accurate estimation of the energy at exit window. These parameter values, along with those for the lateral and angular spread, obtained by computing the beam envelopes, constitute the parametrization of the 150 MeV pencil beam source at the exit window.

The Giraffe depth-dose measurements were not computed for 70 MeV and 240 MeV proton beams, because they are out of the scope of this project and are not further employed. However, the values presented in Tables 4.1 and 4.3 constitute a decent estimate of the pencil beam source parametrization for 70 MeV and 240 MeV proton beams.

4.2. Passive Scattering Fields

Once the fixed pencil beam was characterized, both experimentally and using MC methods, we investigated the properties of the fields produced by the passive scattering system, focusing on a 150 MeV proton beam. Following the approaches described in Section 3.2.3, we studied the uniformity for different field sizes of the lateral beam profiles, computed experimentally. Moreover, we characterized the dose and the dose rate of the passive field.

Lateral beam profiles

The passive scattering system needs to produce different field sizes, depending on the radiobiological application. To achieve this, the distances between the beam-shaping elements play a key role due to the scattering properties of the elements. This section focuses on finding the position between the elements that ensures the system can be used to irradiate fields of different sizes, ranging from $4 \times 4 \text{ cm}^2$ to $20 \times 20 \text{ cm}^2$, guaranteeing a field uniformity of 97%.

As it was described in Section 3.2.3, the best location of the elements was found by analyzing the uniformity of the beam lateral profiles obtained using the Lynx detector. The positions of the dual ring, collimator and detector, all part of the setup presented in Figure 3.3, were optimized. The outcome is presented in Figure 4.9.

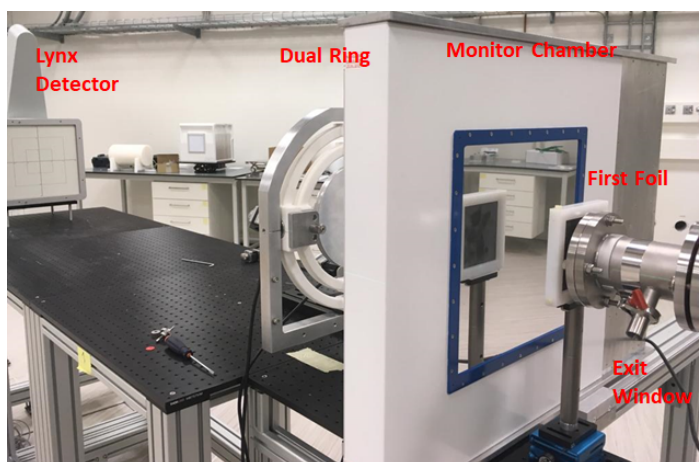


Figure 4.9: Experimental setup in the experimental room for measuring the lateral beam profiles. The beam traverses the exit window and goes through the first foil, monitor chamber and dual ring. Then, the scattered beam reaches the Lynx detector. (Courtesy of A. Ibahimi)

The most appropriate position for placing the dual ring scatterer was found empirically, without including the collimator in the setup. The dual ring scatterer was mounted on a motorized support allowing to precisely align the ring with respect to the beam, in any direction, including forward and backwards. Its best location was found to be at 45 cm from the exit window. Experimentally, we observed that the lateral profiles presented “bunny ears” when the dual ring was too far away from the beam source. This is due to the broadening of the beam which causes the annulus-shaped profile of the outer ring to be predominant.

The effect of having different Lynx positions is presented in Figure 4.10 (200 cm) and Figure 4.11 (250 cm). A larger uniform field was obtained when placing the detector further away from the dual ring, because the

beam scatters more. However, for the same conditions, a closer target captures more signal. A slight misalignment of the beam with respect to the dual ring can be observed in the lateral profiles, given by the higher intensity region on the right of the y-profile and on the left of the x-profile.

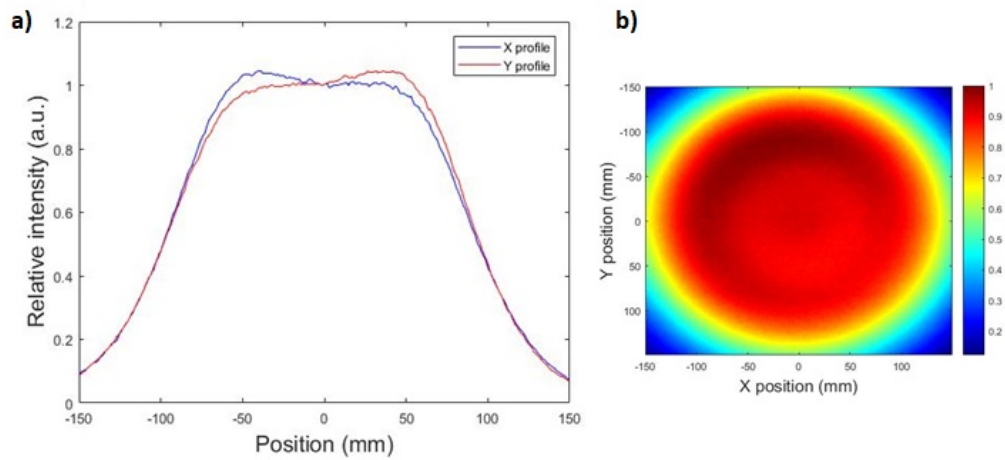


Figure 4.10: Measured irradiated field using the passive scattering setup depicted in Figure 4.9 with the Lynx detector at 200 cm from exit window, computed using the procedure described in Section 3.2.3. a) X-Y lateral profiles, b) 2D intensity map.

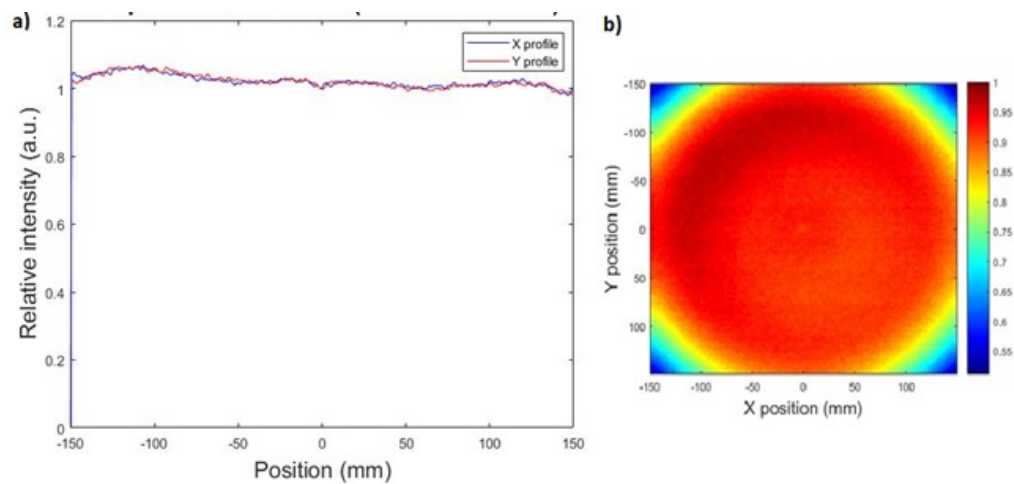


Figure 4.11: Measured irradiated field using the passive scattering setup depicted in Figure 4.9 with the Lynx detector at 250 cm from exit window, computed using the procedure described in Section 3.2.3. a) X-Y lateral profiles, b) 2D intensity map.

The uniformity results for different field sizes of the x-y integral lateral profiles, measured with the setup in Figure 4.9 and computed following the approach described in Section 3.2.3, are presented in Table 4.5. There is a 98%-pixel intensity uniformity in the lateral profiles for a diameter of 12 cm, and 97% for a diameter of 20 cm. Those results are in agreement with the expected outcome and with literature, allowing the use of passive fields for radiobiological irradiation.

Table 4.5: Lateral profile uniformity (x and y) and average uniformity for different field diameters, computed using the procedure described in Section 3.2.3. The intensity uncertainty is not provided by the Lynx manufacturers.

Field Diameter (cm)	Uniformity X (%)	Uniformity Y (%)	Uniformity Avg (%)
5	98	99	99
10	99	99	99
12	99	98	98
16	98	97	98
20	97	96	97
24	97	96	96

The 5 x 5 cm² PMMA collimator was then placed in the beamline with the goal of laterally conforming the dose to this region (Figure 3.4). By evaluating the lateral uniformity at different positions, the optimal location of the collimator was found to be at 187 cm from the exit window. Figure 4.12 presents the x-y lateral profiles for this setup.

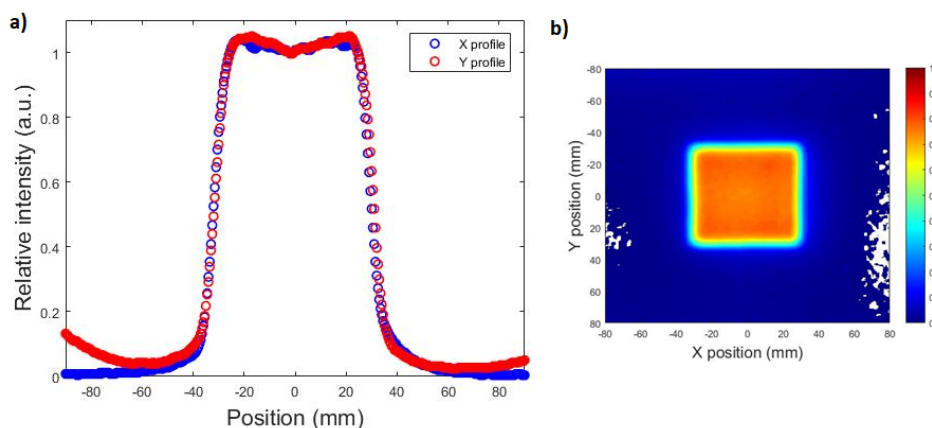


Figure 4.12: Measured irradiated field using the passive scattering setup with the Lynx detector at 200 cm and the collimator at 187 cm from the exit window, computed using the procedure described in Section 3.2.3. a) X-Y lateral profiles, b) 2D intensity map.

A uniformity of 97% for a 5x5 cm² field size was found. Nevertheless, the collimated field needs to be improved by adjusting the alignment of the beamline elements and changing the distance from the dual ring. One effect that can be seen with the collimator is the multiple Coulomb interactions occurring when the protons interact with the collimator slits. This effect is called “slit scattering effect”. The high signal in the Y-profile outside the 5x5 cm² field needs to be investigated, probably coming from beam misalignment.

Relative dose measurements

In order to perform radiobiological experiments, the dose and the dose rate of the passive field need to be characterized. In this section, we present the results of evaluating the dose measured at target for different beam intensities for a 150 MeV mono-energetic proton beam. Moreover, this passive system was tested with 3 additional energies to investigate the robustness of the system.

As it was described in Section 3.2.3, the dose of the field was first measured without any collimation system and the field uniformity was compared with the Lynx measurements. The MatriXX was used for this set of measurements. Table 4.6 summarizes the most relevant uniformity values without collimator. RW3 water slabs were placed in front of the detector in order to measure the dose at the plateau region of the Bragg curve. The table reports the total uniformity for different field sizes at a depth of 5 cm. A 4,5 x 4,5 cm² area shows a uniformity of the integrated lateral profiles of 99%, and a 10 x 10 cm² area has a promising value of 97%. These results agree with those reported in Table 4.5 for the field uniformity found using the Lynx detector. Slight uniformity differences can be attributed to the reproducibility of the setups and the change in detectors. Moreover, the dose was measured for different nominal beam intensity in order to measure the dose rate.

Table 4.6: Uniformity of the lateral dose profiles computed with MatriXX device using the procedure in Section 3.2.3, for the passive scattering system without collimator, for different field sizes ($4,5 \times 4,5 \text{ cm}^2$, $8 \times 8 \text{ cm}^2$, $10 \times 10 \text{ cm}^2$) and intensity, computed at the Bragg peak plateau (5 cm WET). The uniformity uncertainty comes from that of the MatriXX detector (0,5 %).

Energy (MeV)	Intensity (nA)	Time (sec)	Collimator	WET	U (%) $4,5 \times 4,5 \text{ cm}^2$	U (%) $8 \times 8 \text{ cm}^2$	U (%) $10 \times 10 \text{ cm}^2$
150	250	60	No	5 cm	98,7	96,9	96
150	500	60	No	5 cm	99	97,6	97
150	795	60	No	5 cm	99	97,8	97

The dose deposited in the target, after traversing all the beam-shaping elements presented in Figure 3.4, was then analyzed. Therefore, the PMMA pre-collimator and brass collimator system with a $5 \times 5 \text{ cm}^2$ aperture was added to the beamline. Figure 4.13 presents the measured x-y lateral profiles, showing how the alignment of the beam-shaping elements and symmetry is adequate.

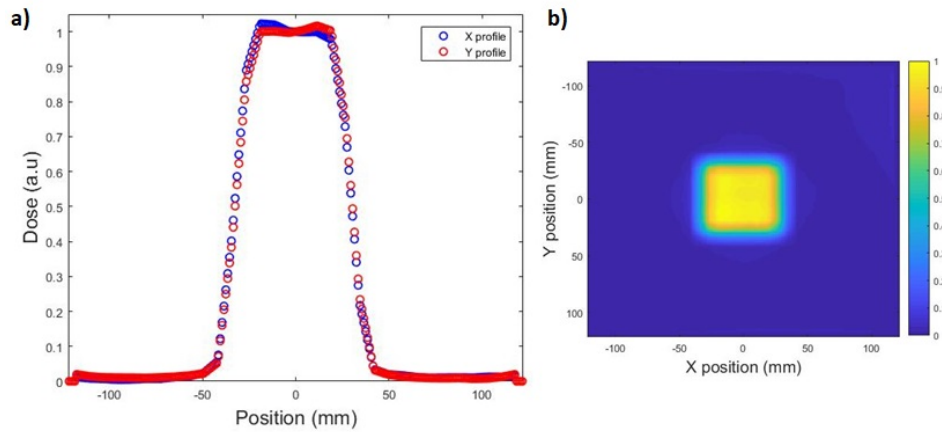


Figure 4.13: Measured dose field using the passive scattering setup depicted in Figure 15 with the Lynx detector at 200 cm and the PMMA + brass collimator at 187 cm from the exit window. The resolution is 1% of the dose and 1 mm a) X-Y lateral profiles, b) 2D intensity map.

Table 4.7 summarizes the uniformity values when placing RW3 slabs to measure the dose at different Bragg curve positions, for the same energy: entrance plateau (5,6 cm of RW3), Bragg peak (9,5 cm to 9,9 cm of RW3) and distal fall-off (10,4 cm of RW3). The difference in total dose for these three different regions is reflected in the increase in the average field dose registered in the Bragg peak area. Following this approach, the Bragg peak was found at a water depth of 9,7 cm with 1 mm resolution. Furthermore, the uniformity in the $4 \times 4 \text{ cm}^2$ field is of around 98% in most cases, with similar values in both x and y integrated lateral profiles, indicating symmetry.

Table 4.7: Dose rate measurements with MatriXX device and lateral profiles uniformity in a $4 \times 4 \text{ cm}^2$ field, computed using the procedure in Section 3.2.3 using the collimated passive system (PMMA+Brass) and changing the WET before, i.e. measurement position in Bragg curve. The uniformity and dose uncertainty comes from that of the MatriXX detector (0,5 %).

E (MeV)	I (nA)	Time (sec)	WET	U (%) - X	U (%) - Y	U (%) - Avg	Dose (Gy)
150	250	60	5,6	99	98,5	98,75	0,15
150	250	60	9,5	98,7	98,6	98,6	1,07
150	250	60	9,7	98,5	98,5	98,5	1,15
150	250	60	9,9	98,3	98,3	98,3	1,00
150	250	60	10,4	97,7	97,5	97,6	0,14

Table 4.8 collects the dose measurements resulting from shooting the beam for a minute, for different energies and a fixed intensity value (795 nA). The total uniformity in the irradiated $4 \times 4 \text{ cm}^2$ area is higher than 97% in all cases. The symmetry between x and y profiles is also appropriate, with differences of less than 1% uniformity among the two, which are within the uncertainty. Moreover, for higher doses, higher uniformity is generally reached. The reason is that higher dose leads to an improvement in the signal-to-noise ratio in the detector because the detected signal is higher.

These experiments confirm the possibility of conforming the lateral spread using the passive scattering system with a collimator for obtaining a homogeneous lateral dose with a defined penumbra. In this case, using

Table 4.8: Dose measurements with MatriXX device and lateral profiles uniformity in a $4 \times 4 \text{ cm}^2$ field, computed using the procedure in Section 3.2.3, for different beam energies, using the collimated passive system (PMMA+Brass). The uniformity and dose uncertainty comes from that of the MatriXX detector (0,5 %).

E (MeV)	I (nA)	Time (sec)	WET	U (%) - X	U (%) - Y	U (%) - Avg	Dose (Gy)
115	795	60	No slabs	96,8	97,6	97,2	0,41
130	795	60	No slabs	97,9	97,8	97,8	0,62
140	795	60	No slabs	98,3	97,8	98	0,86
150	795	60	No slabs	98,1	97,7	97,9	1,18

a PMMA pre-collimator and brass collimator with an aperture of $5 \times 5 \text{ cm}^2$, for various energies. For a nominal energy of 150 MeV, a uniformity of 98% is achieved for the lateral profiles in a $4 \times 4 \text{ cm}^2$ target in the Bragg peak region, with symmetry in the x and y direction. As mentioned in the previous section, an improvement of the passive scattering beamline alignment will potentially increase the uniformity further, reaching the same values as when using the uncollimated beam (more than 99% uniformity). Moreover, a good uniformity was obtained also for different energies, which shows the robustness of the setup. Furthermore, experiments with no collimator in place prove that the optimized system is prepared to irradiate larger fields using a collimator with a larger aperture, once the best alignment is achieved.

4.3. Comparison of Experimental Data vs TOPAS Simulations for the Passive Scattering Setup

Once the pencil beam simulations were benchmarked and the beam source parameters were estimated, we compared the MC simulations of the passive scattering system with the experimental data, following the procedures described in Section 3.3.4. We benchmarked the system by evaluating the lateral field profiles and their uniformity, the Bragg curves, and the dose distributions.

Depth-dose distributions

Depth-dose distributions of the passive scattering system were used for benchmarking the MC model. The main goals for using them was to validate the beam source parameters, the geometrical model and physics model details used in the MC code. In this section, we present, compare, and discuss the experimental and simulated pristine Bragg peaks and SOBP.

Pristine Bragg peak

Pristine Bragg curves were simulated using the TOPAS passive scattering setup depicted in Figure 3.7, with a scoring volume and following the procedure described in Section 3.2.3. This model was implemented in such a way that it reproduced the same beamline elements and the distances between them, found in Section 4.2.

The beam source parameters used as input of the MC simulations were initially set to those found for the pencil beam, reported in Section 4.1. Then, to find the agreement between the simulated passive beamline and the measurements, for a 150 MeV nominal proton beam, the mean energy and energy spread were further tuned to 149.1 MeV with an energy spread of 0.95%, as summarized in Table 4.9. Figure 4.14 presents the comparison between the experimental and simulated depth-dose curves, for a proton beam with a nominal energy of 150 MeV. As it can be observed, there is good agreement between both ranges and distal fall-off.

Table 4.9: Initial energy and energy spread used as input for the simulation to achieve agreement with measured d20-d80 (distal fall-off) and d80 (range) pristine Bragg curve values of the passive scattering system, for a nominal energy of 150 MeV. Simulation for 10^7 proton histories. The uncertainty of the measurements and simulations is of 0,25 mm and 0,5 mm, respectively.

	Initial Energy (MeV)	Energy Spread (%)	d20-d80 (cm)	d80-range (cm)
Simulation	149,1	0,94	0,43	10,39
Measurement	150,1	-	0,42	10,37

This tuning procedure is widely reported in literature (Section 2.2.1). The main reason why the values need to be tuned after adding all the elements in the beamline is that the modelling of the elements introduces inaccuracies in the simulation due to:

- The information provided by their manufacturers about the geometry and composition of the element is an estimation

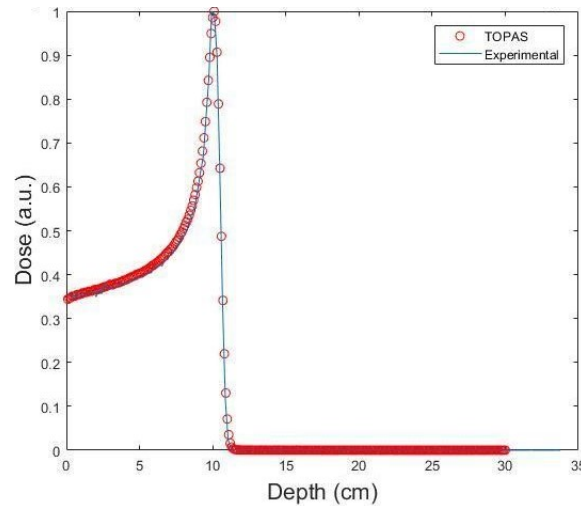


Figure 4.14: Experimental (blue) pristine Bragg curve for 150 MeV proton beam (nominal energy) and simulated pristine Bragg curve with the passive scattering system. The simulation input parameters are: initial energy 149,1 MeV, energy spread 0,94%, and lateral and angular spread as specified in Table 4.1. The uncertainty of the measurements and simulations is of 0,25 mm and 0,5 mm, respectively. Simulation for 10^7 proton histories.

- The mean ionization potentials of the element's materials are not tuned, and the default values provided by TOPAS are used
- The Giraffe detector is modelled as a water tank, disregarding the elements and physics processes to obtain the dose deposition.

By tuning the initial mean energy, energy spread and fixing these values for future simulations using this setup, it is therefore possible to disregard these sources of inaccuracy. Table 4.10 collects the beam source parameters for both the pencil beam in air and the ones corrected for the presence of the beamline elements.

Table 4.10: Beam source parameters for a 150 MeV proton beam in air and after traversing all the elements of the passive system (correction applied).

	Initial Energy (MeV)	Energy Spread (%)	Lateral Spread (cm)	Angular Spread (rad)
In air	150,2	0,85	0,27 (x)	0,0027 (x)
			0,21 (y)	0,0032 (y)
Passive System	149,1	0,94	0,27 (x)	0,0027 (x)
			0,21 (y)	0,0032 (y)

Depth-dose curves obtained using the same setup were experimentally obtained for different nominal energies. Those measurements were performed to test the robustness of the setup for different energies than the optimized one (150MeV). The first four rows in Table 4.11 gather the experimental conditions and the results.

Table 4.11: Bragg peak measurements using the Giraffe detector after the passive scattering system. The first four rows do not include ridge filter while the last one does. The range uncertainty is of 0,25 mm, given by the Giraffe resolution.

Ridge Filter	Nominal Energy (MeV)	nA	d80 (cm)	d20 (cm)	Energy at Target (MeV)
No	150	350	10,43	10,04	118,6
No	140	350	8,66	9,04	106,77
No	130	350	6,96	7,3	94,4
No	115	350	4,58	4,96	74,7
Yes	150	350	10,05	-	116,1 (max)

Spread-out Bragg peaks

Spread-Out Bragg peak measurements have been performed including the ridge filter in the passive scattering system. The experimental setup is shown in Figure 3.3. The goal of this measurement is to evaluate the uniformity and width of the spread-out Bragg peak for a field in order to be able to irradiate volume.

Table 4.11 gathers the experimental conditions and the information of the measured depth-dose curve presented in Figure 4.15. The uniformity of the SOBP was evaluated for different widths in order to check the field homogeneity in the longitudinal direction. As we report in Table 4.12, the uniformity is higher than 98.6% for a width of up to 3.4 cm. This means that the given passive scattering system, including the chosen ridge filter, can be used to homogeneously irradiate target volumes.

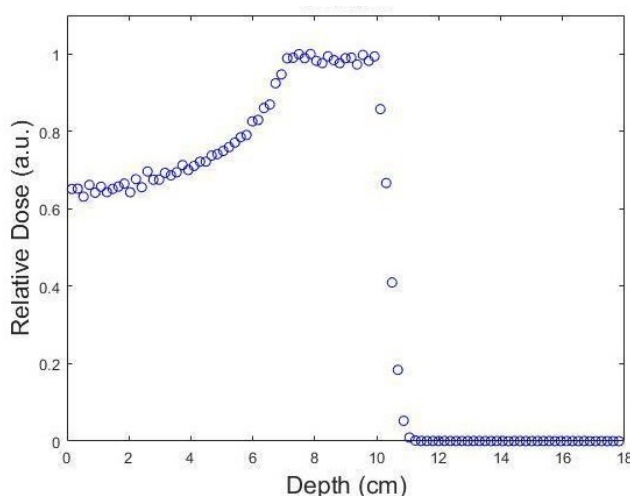


Figure 4.15: Experimental Spread Out Bragg Peak for a 150 MeV proton beam (nominal energy). The range uncertainty is of 0,25 mm, given by the Giraffe resolution.

Table 4.12: Uniformity (%) of the spread out bragg peak, for different modulation widths.

Modulation Width (cm)	3,4	2,1	0,9
Uniformity (%)	98,6	98,6	98,7

Once the SOBP measurements were obtained, a benchmark of the SOBPs was attempted with the model implemented in TOPAS. Results are shown in Figure 4.16. The distal fall-off is properly represented, however, the entrance channel and the beam modulation do not follow the experimental data distribution. One of the possible explanations for this disagreement is the dimension of the integration volume where the simulation has been performed. Benchmarking the ridge filter system with the large field could show, in fact, the distortion of the beam on the edges of the ridge filter. The simulation seems to be sensitive to the edge effects which are accounted for in the integrated volume. In this case, the SOBP simulations could be improved by reducing the lateral dimensions of the scoring volume. Moreover, it is possible that the design of the ridge filter is slightly different than the simulated one in terms of type of material. Time limitations did not allow to perform further implementations in this thesis.

Lateral beam profiles

The benchmark the lateral beam profile of the large fields is important to test the accuracy of the implemented geometry and the model of the beam interactions with the dual ring setup. The simulations were all performed using 3×10^7 primary protons, unless stated otherwise.

As it was described in Section 3.3.4, we use two methods to process the dose profiles simulation raw data: the direct approach and the radial projection approach. Figure 4.17 compares the result of following both approaches for an uncollimated beam, for the same number of proton histories. As described in Section 3.3.4, the radial projection method generates a symmetric lateral profile, i.e. each ring has a single value gathering both the original values from the positive and negative side of the lateral profile axis. For illustration purposes, we mirror the projected values in the figures. It can be readily observed that the radial projection method, which has 75 rings in this case, reduces the statistical uncertainty of the lateral profiles. Using the direct approach, which directly plots the central profiles, the standard error is in the order of 4%. On the other hand, the radial projection method significantly reduces the statistical uncertainty by $\frac{1}{\sqrt{\text{number of voxels in ring}}}$. Given the computational and time resources available, this approach was chosen to process the simulated

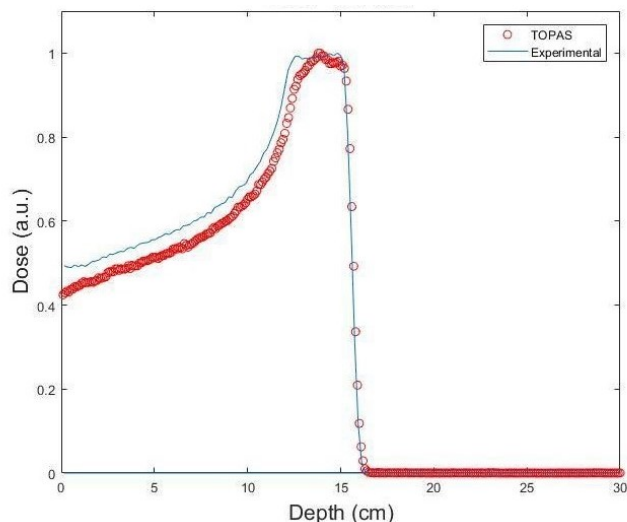


Figure 4.16: Experimental (blue) and simulated (red) Spread Out Bragg Peak for 150 MeV proton beam (nominal energy) with the passive scattering system. The simulation input parameters are specified in Table 4.10 for the passive system. The uncertainty of the measurements and simulations is of 0,25 mm and 0,5 mm, respectively. Simulation for 10^7 proton histories.

data and to extract the lateral beam profiles.

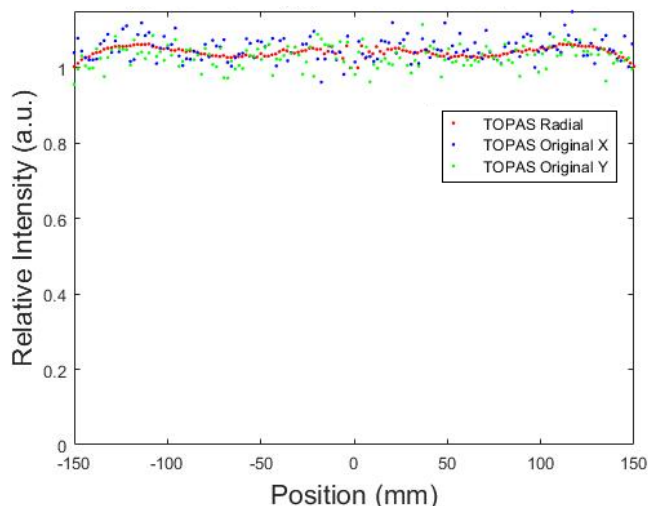


Figure 4.17: Comparison between the two approaches for processing simulated lateral beam profiles of a passive scattering system: radial projection method with 75 rings (red) and direct method (blue-x and green-y). The uncertainty using the direct method, obtained from TOPAS, is in the order of 4%. Simulations were performed for 3×10^7 primary protons.

The comparison of the simulated and measured lateral x and y-profiles for an uncollimated passively scattered beam are depicted in Figure 4.18. Both curves are normalized to the center value. As it can be observed, the measurements show a slight misalignment due to the beam position with respect to the dual ring system. However, the field size is properly reproduced by the simulations.

Equation 3.1 was used to quantify the uniformity of the integral lateral profiles. The radial projection sums the values of the voxels contained in each ring; therefore, this approach does not distinguish between x and y profile. Moreover, for computing the uniformity, the two central rings were not accounted for. The reason is that the statistical uncertainty is higher in that region due to the lower number of voxels included in each ring. Table 4.13 compares the measured and simulated uniformity values for various field sizes. The agreement between both results validates the simulation model without collimator.

Both processing methods were also used to evaluate the lateral profiles of the setup using the collimator.

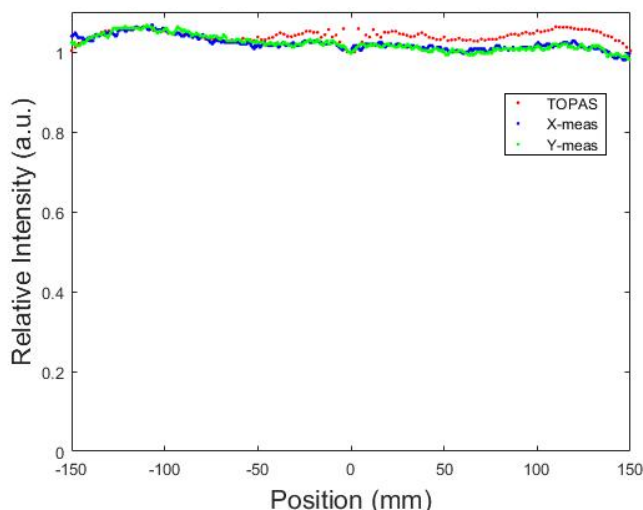


Figure 4.18: Comparison between experimental (blue-x, green-y) and simulated lateral profiles computed using the radial projection approach with 75 rings. Simulations were performed for 3×10^7 primary protons.

Table 4.13: Comparison of uniformity of lateral profiles (x-y) for measurements (Lynx) and simulations, for different field sizes, after the uncollimated scattering system. The simulation uncertainty comes from averaging the error provided by TOPAS over the region of interest

		5X5 cm ²	10x10cm ²	16x16cm ²
EXPERIMENTAL (%)	x	98,7	98,6	98,6
	y	98,3	98,3	98
SIMULATION (%)		98,4 ± 0.7	98,4 ± 0.5	98,4 ± 0.4

Figure 4.19 presents the measured and simulated 2D dose profiles for the complete setup with collimator.

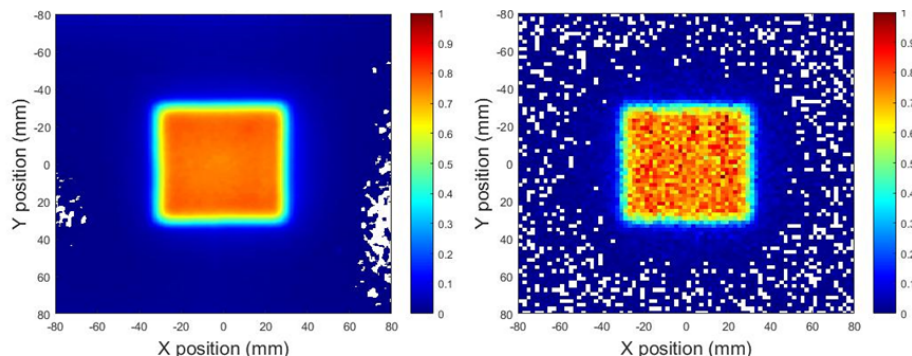


Figure 4.19: Measured (left) and Simulated (right) 2D dose profiles for a 150 MeV proton beam going through the passive scattering system with collimator. Simulations were performed for 3×10^7 primary protons.

Figure 4.20.a compares measurements and simulations processed with the radial projection method. In this case, although the statistical uncertainty is improved, the lateral penumbra does not match the measured one. The capability of spatial location of the penumbra decreases because the collimator has a squared shape and the voxels are grouped together in circular rings. This causes incorrect approximations in the rings including the collimator edges. Nevertheless, for a collimator of 5×5 cm² these simulations can be used to find an approximation of the uniformity for the inner circle with a radius of 25 mm (Table 4.14).

On the other hand, Figure 4.20.b presents the comparison between measured and simulated profiles, using the direct processing approach. In this case the comparison shows a good lateral penumbra agreement, even considering the statistical fluctuations in the values of the irradiated field.

Given this, the radial project method is a processing method that should be carefully used. Its main advantage is that for a given number of primary protons and a given scorer grid, it greatly reduces the statistical

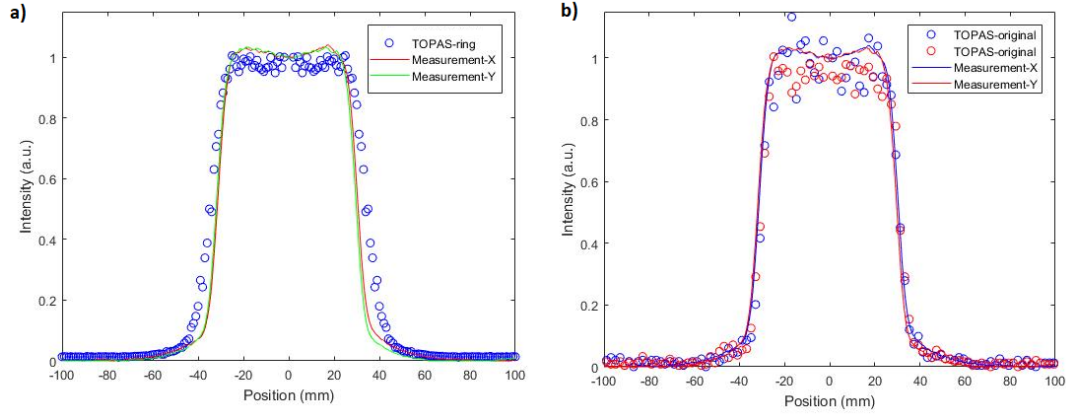


Figure 4.20: Comparison of x-y lateral profiles for measurements (Lynx, solid lines) and simulations (circles), after the collimated passive scattering system. A) Simulated lateral profiles processed using the radial projection method for 150 rings (error: 1,3%) b) Simulated lateral profiles processed using the direct approach (average error: 4.7%). Simulations were performed for 3×10^7 primary protons.

Table 4.14: Comparison of uniformity of lateral profiles (x-y) for measurements (Lynx) and simulations, for a $5 \times 5 \text{ cm}^2$ field, after the collimated passive scattering system. The simulation uncertainty comes from averaging the error obtained after performing the radial projection method, over the region of interest.

		5X5 cm²	
Experimental (%)	x	96,7	
	y	96,1	
Simulation (%)		97,1 ± 1,3	

uncertainty of a simulation as compared to the direct processing method. This is useful in situations when there are time and computational constraints, such as this work, where simulating a very high number of histories or using a grid with small voxels will be too much time consuming. However, this method assumes that the beam is symmetrical while the experiment shows a slight beam asymmetry. Another aspect to consider of this approach is the resolution with respect to the conventional method. The resolution, in fact, depends on the number of rings in which the grid is divided, e.g. for a $30 \times 30 \text{ cm}^2$ surface and an original grid of 150×150 voxels, 150 rings will have the same resolution as the original, but 75 rings will half the original resolution.

In conclusion, it was observed that the passive scattering TOPAS model of the beamline properly models both the physics processes and collimator, revealing the ability of the TOPAS model to reproduce the passive scattering system and model the behavior of the passive beamline in different scenarios.

Dose distribution

The MC model of the passive scattering beamline can be used to estimate the dose deposited in the target area, as well as its uniformity. This procedure is described in Section 3.3.4. In this section, simulations were first used to estimate the number of protons required to deposit a given dose in the target and the location of the Bragg peak. In this way, it was possible to have an estimation on the required intensity and irradiation time of the beam to reach a certain dose. Moreover, the simulations were used to provide an estimation of the dose uniformity in the target.

Estimating number of initial protons

The first step was to correlate the dose value in the target area with the initial number of protons. This was done using experimental data measured at HPTC which relate each nominal energy to the number of protons irradiated per second per 1 nA. The results are reported in Table 4.15.

The experimental mean deposited dose in one of the areas of interest for a one-minute irradiation at 500 nA nominal intensity of 150 MeV, was 2,09 Gy. This constitutes $6,06 \times 10^{11}$ irradiated protons. For the simulation with 10^6 primary protons, the mean dose in the area of interest was of $2,56 \times 10^{-6}$ Gy. Based on the experimental data and by a simple rule of three, it was expected to need to simulate $8,18 \times 10^{11}$ initial protons to obtain the same experimental dose. This over estimation is confirmed for all the results compared in Table 4.15,

Table 4.15: Correlation of the simulated and measured dose values in the target area with the initial number of simulated primary protons and initial protons given the measured number of protons per second per 1 nA.

Primary Protons	Sim Dose (Gy)	Meas Dose (Gy)	E (MeV)	Protons/s per 1 nA (nom)	I (nA)	Time(s)	Meas Protons	Sim Protons
10^6	$2,56 \times 10^{-6}$	1,09	150	$2,02 \times 10^{-8}$	250	60	$3,03 \times 10^{11}$	$4,27 \times 10^{11}$
10^6	$2,56 \times 10^{-6}$	2,09	150	$2,02 \times 10^{-8}$	500	60	$6,06 \times 10^{11}$	$8,18 \times 10^{11}$
10^6	$2,56 \times 10^{-6}$	3,45	150	$2,02 \times 10^{-8}$	795	60	$9,64 \times 10^{11}$	$1,35 \times 10^{12}$

as shown in Figure 4.21. The difference between expected and measured values is probably related to the provided measurement data from which the calculation from a nominal current was made. The agreement is expected to improve if the real number of protons had been measured during the experiment. Moreover, the number of simulated histories is low; therefore, its uncertainty is high. Increasing the number of primary protons simulated would also probably increase the accordance.

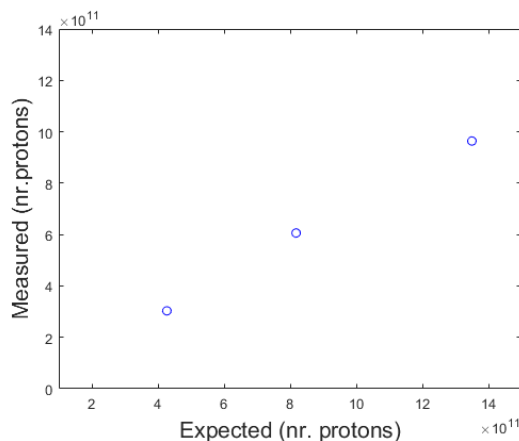


Figure 4.21: Comparison between expected (simulated) and measured number of protons for the simulation and experimental data given in table 4.15. Simulations were performed for 10^6 primary protons.

Estimating the location of the Bragg peak

MC simulations were employed to evaluate whether we could estimate the location of the Bragg peak. To achieve that, water slabs of different thickness were placed in front of the scorer. For each simulation, we simulated 6×10^6 primary protons and scored the mean dose deposited in the central $4 \times 4 \text{ cm}^2$ field. The statistical uncertainty in the target area ranged between 17-28%. Figure 4.22 presents the results obtained; using the simulations, the Bragg peak is found at 10 cm. This is a 3 mm shift with respect to experimental data (Table 8). This shift can be due to the ionization potential and the atomic composition used for reproducing the water slabs, as discussed in Sections 1.1.1 and 4.1. Moreover, the simulation uncertainty is very high: choosing a higher number of initial proton histories, this method could be used to perform accurate estimations.

Validating dose lateral profiles

Simulations of the lateral dose beam profiles have been performed and benchmarked against the experimental data. The power of the model to reproduce the data would allow to perform simulations prior any experiments to estimate dose uniformity.

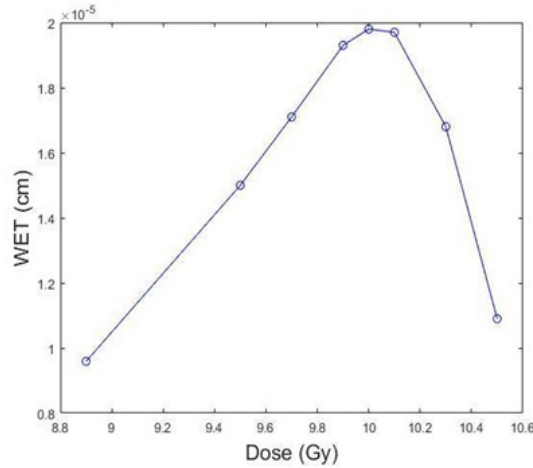


Figure 4.22: Variation of the simulated dose for a passive scattering system when placing blocks with different water equivalent thicknesses before the scoring surface. The highest peak corresponds to the location of the Bragg peak. The dose uncertainty ranges 17-28%. Simulations were performed for 6×10^6 primary protons.

Figure 4.23 compares the lateral profiles of both the measurements and the simulations. 3×10^7 primary protons were used in the MC simulations. The lateral dose penumbra is properly modeled, which means the collimator modeling and the simulated physics processes were appropriate. However, it can be observed that the statistical uncertainty is high in the collimated target area. The average error in the collimated area is of 7%, for both x-y profiles. This behavior is similar to the one presented for the lateral beam profiles that score the number of particles arriving to the target.

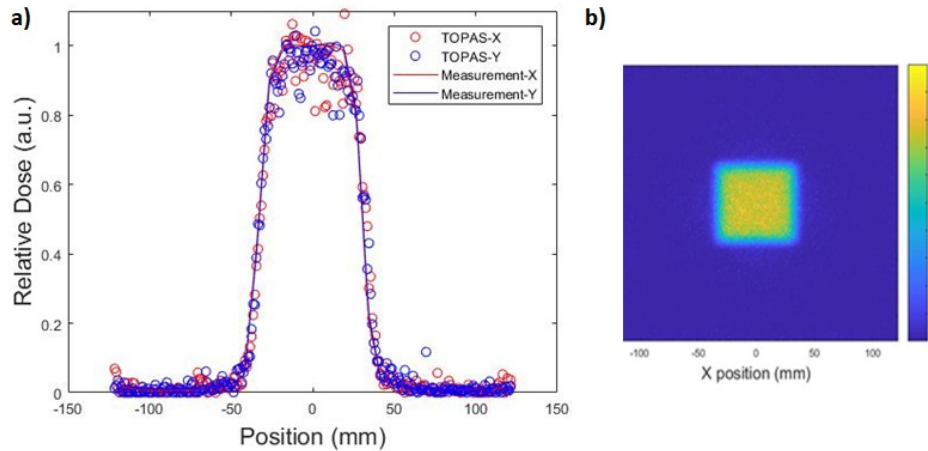


Figure 4.23: Comparison of measured and simulated irradiated dose fields using the passive scattering setup depicted in Figure 15. a) Comparison of x-y lateral Dose profiles of measurements (solid lines) and simulations (circles), processed using the direct approach (average error: 4.7%) b) Measured 2D dose map for a 150 MeV proton beam. Simulations were performed for 3×10^7 primary protons.

Improving the statistics of the simulation by increasing the number of primary protons simulated is not feasible due to computational and time limitations. To overcome this, we used the radial projection method. Results are presented in Figure 4.24. As it was discussed in the previous subsection, this method reduces the spatial resolution resulting in a shift in the lateral penumbra. However, the approximation in the $4 \times 4 \text{ cm}^2$ target is good enough to compute an estimate of the uniformity values. Table 4.16 shows a comparison of the uniformity values of the measurements and simulations. The value of the two first rings extracted from the radial projection method are excluded. For a $4 \times 4 \text{ cm}^2$ field, there is a 1% difference in the uniformity value of the total field. For a $4.5 \times 4.5 \text{ cm}^2$ field, the simulation outputs a 3% higher uniformity. This difference might be related to the fact that the measurements are slightly misaligned, and that the radial projection method assumes a symmetrical beam.

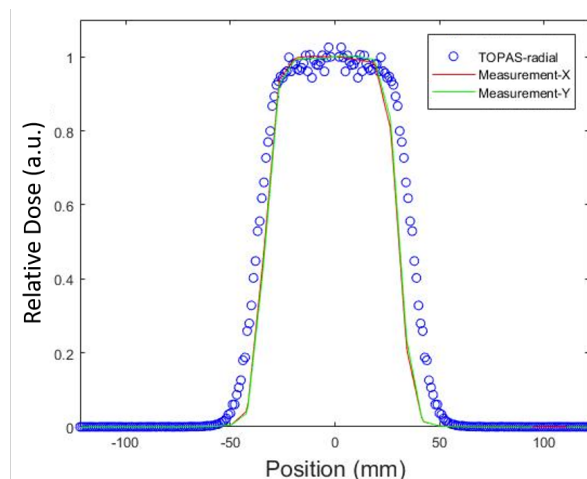


Figure 4.24: Comparison of x-y lateral Dose profiles for measurements (solid lines) and simulations (Blue circles). Simulated lateral profiles processed using the radial projection approach (average error: 1%). Simulations were performed for 3×10^7 primary protons.

Table 4.16: Comparison of uniformity (U) of lateral profiles (x-y) for measurements (MatriXX) and simulations, for different fields, after the collimated passive scattering system. The measurement error is of 0,5%, coming from the MatriXX characteristics, and the simulation uncertainty comes from averaging the error obtained after performing the radial projection method, over the region of interest.

	$4 \times 4 \text{cm}^2$			$4.5 \times 4.5 \text{cm}^2$		
	U (%) X	U (%) Y	Avg U (%)	U (%) X	U (%) Y	U (%)
Measured	98,5	97,8	98,1	96,2	95,9	96
Simulated	-	-	$97,4 \pm 0.93$	-	-	96.5 ± 0.9

In conclusion, the results presented in this section show that the passive scattering TOPAS model can be used to approximate the dose deposition in the target volume using the experimental setup of the HPTC R&D bunker. Therefore, it is a useful tool for assisting in the preparation of radiobiological experiments which require different doses and setups.

5

Conclusions and Future Prospects

Nowadays, there are 104 proton centers around the world and their presence is extensively spreading. The physical advantages of using proton therapy to treat deep-seated tumor lies in the profile of their depth-dose distribution in the tissue. In fact, the more the protons penetrate the tissue the higher is the energy deposition because of slow-down electromagnetic processes. On the contrary, photons have the opposite behavior depositing the highest dose at the tissue entrance. For this characteristic, protons are considered one of the best candidates for specific tumor classifications, in order to spare healthy tissues and have higher radiobiological effectiveness in the tumor volume. Nevertheless, to show the added value of proton therapy, to apply research-driven care to patients and to develop next generation treatments, all the radiobiological mechanisms have to be fully understood.

One of the purposes of the research program of HollandPTC (HPTC) is to perform clinical trials as well as pre-clinical experiments on cells and animals. For the latter, HPTC dedicated a proton experimental beamline and three laboratories. The experimental room is equipped with a fixed horizontal beamline providing a single pencil beam. In order to conduct different radiobiological experiments, the beamline needs to be equipped to provide large field irradiation with an accurate dose characterization.

In this context, the two main goals of this master thesis project were: to implement a passive dual ring scattering system in the experimental room of HPTC to produce homogeneous fields of different sizes; to create a MC model of the HPTC passive scattering beamline able to reproduce the experimental setup. Therefore, this project includes experimental work, performance of Monte Carlo (MC) simulations and processing of raw data.

The dual ring passive scattering system implemented throughout this work was optimized for a 150 MeV mono-energetic initial beam allowing to:

- Study the experimental condition to produce a $4 \times 4 \text{ cm}^2$, $10 \times 10 \text{ cm}^2$, $16 \times 16 \text{ cm}^2$ and $20 \times 20 \text{ cm}^2$ passive field.
- Achieve for every field size uniformity between 96% and 99%, for the largest field to the smallest, respectively.
- Prove the feasibility of the experimental design, its reliability and its robustness in producing homogeneous fields.
- Produce a collimated field of $4 \times 4 \text{ cm}^2$ with up to 97% uniformity.
- Validate the passive ridge filter to produce Spread-Out Bragg peaks of 3 cm width and up to 98% uniformity.
- Show the adaptation of the setup for different beam initial energies.
- Evaluate the energy loss in the passive beam element in order to measure the proton energy of the field (at target position).

The development of a MC model using TOPAS was performed in parallel to the experimental work during the thesis project.

In the first part of the MC project, the pencil beam had to be simulated and compared to the data in order to produce the initial parameters to the passive field setup. In this context, the model reproduced the depth-dose curves and the lateral beam profiles at different positions in air, giving as output the lateral spread, the angular spread, the energy spread and the mean energy of the HPTC proton beam.

For the depth-dose distribution of pristine Bragg peaks, a millimetric agreement was found between data and simulations. The lateral beam spot profiles of the single pencil beam agreed inside the experimental error.

In the second part of the simulation work, the beam characteristics passing through the beam-shaping elements were reproduced. For this case, not only the depth-dose curves were compared with the experimental data, showing the different energy at target position, but also the lateral profiles of the large fields were studied. The agreement between data and simulation was successful. Agreement was found for the uniformity of the lateral profiles and the lateral penumbra of the collimated beam. The radial projection method was implemented as an alternative to process the lateral profiles which significantly reduces the statistical uncertainty with respect to the conventional processing method, at expenses of loss in resolution.

An attempt of simulating the ridge filter data was made in this work. However, a disagreement between simulation and experimental measurements was found. The simulated distribution did not show a distribution as flat as the data. This behavior could be attributed to some distortion effects of the beam at the edge of the ridge filter increased by the presence of the passive setup and the collimator. To have a better idea of this behavior, different simulations have to be performed, reducing the scoring volume dimensions, with passive setup and without. The latter were not part of this work.

The dose of the field was measured with a quality assurance clinical device, the MatriXX. The average dose value over a field of 4x4cm² at different Bragg peak positions was studied. The TOPAS model attempted to simulate the average field dose to perform a comparison. It was found an underestimation of the number of protons with respect to the expected ones. The disagreement can be referred to an uncertainty of the estimated total amount of protons sent during the measurement. The latter was, in fact, estimated by table values and not directly measured during the experiment.

Throughout this project, the dual-ring passive scattering setup has been successfully implemented in the experimental room of HPTC to have different sizes for different applications. This setup is ready to be used in radiobiological experiments. Moreover, a TOPAS MC model of the passive scattering system has been created that can provide an estimation of the pencil beam parameters at exit window, and that is benchmarked against experimental data. This model can be used to assist in the preparation of radiobiological experiments and to further optimize the beamline design. All in all, the goals of this master thesis project have been successfully reached.

As a follow-up to the conclusions and to increase the usefulness of the beamline in the near future, we suggest the following:

- Improving the alignment of the beam-shaping elements and the distance between the collimator to increase the uniformity of the collimated field.
- Manufacturing and introducing collimators with different aperture sizes to conform the lateral dose to different target areas.
- Computing absolute dose values to precisely know the dose arriving to the target.
- Measuring the lateral dose profiles at different regions of the SOBP to evaluate the beam lateral spread along the beam axis direction.
- Performing dose measurements in x-y-z of the fields inside a water phantom.
- Creating fields with sizes smaller than 5x5 cm² with a thinner dual ring setup increasing the dose rate.

In order to improve the MC model, we recommend:

- Improving the ridge filter model and simulation to achieve good agreement between experimental and simulated spread-out Bragg peaks.

- Running the lateral beam simulations with a very large number of primary protons to reduce the statistical uncertainty of the scores without requiring additional data processing.
- Simulating the lateral dose profiles at different regions of the SOBP and using the experimental data to benchmark the model of physics interactions caused by the presence of the collimator, i.e. slit scattering effect.
- Using the TOPAS model to perform neutron dose estimation caused by the beam-shaping elements, beneficial for radiation protection purposes.

Bibliography

- [1] S. Agostinelli, J. Allison, K. Amako, J. Apostolakis, H. Araujo, P. Arce, M. Asai, D. Axen, S. Banerjee, G. Barrand, F. Behner, L. Bellagamba, J. Boudreau, L. Broglia, A. Brunengo, H. Burkhardt, S. Chauvie, J. Chuma, R. Chytraccek, G. Cooperman, G. Cosmo, P. Degtyarenko, A. Dell'Acqua, G. Depaola, D. Dietrich, R. Enami, A. Feliciello, C. Ferguson, H. Fesefeldt, G. Folger, F. Foppiano, A. Forti, S. Garelli, S. Giani, R. Giannitrapani, D. Gibin, J.J. Gómez Cadenas, I. González, G. Gracia Abril, G. Greeniaus, W. Greiner, V. Grichine, A. Grossheim, S. Guatelli, P. Gumplinger, R. Hamatsu, K. Hashimoto, H. Hasui, A. Heikkinen, A. Howard, V. Ivanchenko, A. Johnson, F.W. Jones, J. Kallenbach, N. Kanaya, M. Kawabata, Y. Kawabata, M. Kawaguti, S. Kelner, P. Kent, A. Kimura, T. Kodama, R. Kokoulin, M. Kossov, H. Kurashige, E. Lamanna, T. Lampén, V. Lara, V. Lefebure, F. Lei, M. Liendl, W. Lockman, F. Longo, S. Magni, M. Maire, E. Medernach, K. Minamimoto, P. Mora de Freitas, Y. Morita, K. Murakami, M. Nagamatu, R. Nartallo, P. Nieminen, T. Nishimura, K. Ohtsubo, M. Okamura, S. O'Neale, Y. Oohata, K. Paech, J. Perl, A. Pfeiffer, M.G. Pia, F. Ranjard, A. Rybin, S. Sadilov, E. Di Salvo, G. Santin, T. Sasaki, N. Savvas, Y. Sawada, S. Scherer, S. Sei, V. Sirotenko, D. Smith, N. Starkov, H. Stoecker, J. Sulkimo, M. Takahata, S. Tanaka, E. Tcherniaev, E. Safai Tehrani, M. Tropeano, P. Truscott, H. Uno, L. Urban, P. Urban, M. Verderi, A. Walkden, W. Wander, H. Weber, J.P. Wellisch, T. Wenaus, D.C. Williams, D. Wright, T. Yamada, H. Yoshida, and D. Zschesche. Geant4—a simulation toolkit. *Nuclear Instruments and Methods in Physics Research Section A: Accelerators, Spectrometers, Detectors and Associated Equipment*, 506(3), July 2003. ISSN 01689002. doi: 10.1016/S0168-9002(03)01368-8. URL <https://linkinghub.elsevier.com/retrieve/pii/S0168900203013688>.
- [2] P. Andreo. Monte Carlo techniques in medical radiation physics. *Physics in Medicine and Biology*, 36(7):861–920, July 1991. ISSN 0031-9155, 1361-6560. doi: 10.1088/0031-9155/36/7/001. URL <https://iopscience.iop.org/article/10.1088/0031-9155/36/7/001>.
- [3] Milad Baradaran-Ghahfarokhi, Francisco Reynoso, Michael T. Prusator, Baozhou Sun, and Tianyu Zhao. Sensitivity analysis of Monte Carlo model of a gantry-mounted passively scattered proton system. *Journal of Applied Clinical Medical Physics*, 21(2):26–37, February 2020. ISSN 1526-9914, 1526-9914. doi: 10.1002/acm2.12803. URL <https://onlinelibrary.wiley.com/doi/abs/10.1002/acm2.12803>.
- [4] N. Bassler, D. C. Hansen, A. Lühr, B. Thomsen, J. B. Petersen, and N. Sobolevsky. SHIELD-HIT12A - a Monte Carlo particle transport program for ion therapy research. *Journal of Physics: Conference Series*, 489:012004, March 2014. ISSN 1742-6588, 1742-6596. doi: 10.1088/1742-6596/489/1/012004. URL <https://iopscience.iop.org/article/10.1088/1742-6596/489/1/012004>.
- [5] Bryan Bednarz, Hsiao-Ming Lu, Martijn Engelsman, and Harald Paganetti. Uncertainties and correction methods when modeling passive scattering proton therapy treatment heads with Monte Carlo. *Physics in Medicine and Biology*, 56(9):2837–2854, May 2011. ISSN 0031-9155, 1361-6560. doi: 10.1088/0031-9155/56/9/013. URL <https://iopscience.iop.org/article/10.1088/0031-9155/56/9/013>.
- [6] Chris Beltran, Yingcui Jia, Roelf Slopsema, Daniel Yeung, and Zuofeng Li. A simplified methodology to produce Monte Carlo dose distributions in proton therapy. *Journal of Applied Clinical Medical Physics*, 15(4):2–10, July 2014. ISSN 1526-9914, 1526-9914. doi: 10.1120/jacmp.v15i4.4413. URL <https://onlinelibrary.wiley.com/doi/abs/10.1120/jacmp.v15i4.4413>.
- [7] David J. Brenner, Carl D. Elliston, Eric J. Hall, and Harald Paganetti. Reduction of the secondary neutron dose in passively scattered proton radiotherapy, using an optimized pre-collimator/collimator. *Physics in Medicine and Biology*, 54(20):6065–6078, October 2009. ISSN 0031-9155, 1361-6560. doi: 10.1088/0031-9155/54/20/003. URL <https://iopscience.iop.org/article/10.1088/0031-9155/54/20/003>.
- [8] M. Bueno, H. Paganetti, M. A. Duch, and J. Schuemann. An algorithm to assess the need for clinical Monte Carlo dose calculation for small proton therapy fields based on quantification of tissue heterogeneity: Assessing the need for Monte Carlo dose calculation for small proton beams. *Medical Physics*,

- 40(8):081704, July 2013. ISSN 00942405. doi: 10.1118/1.4812682. URL <http://doi.wiley.com/10.1118/1.4812682>.
- [9] Kwangzoo Chung, Jinsung Kim, Dae-Hyun Kim, Sunghwan Ahn, and Youngyih Han. The proton therapy nozzles at Samsung Medical Center: A Monte Carlo simulation study using TOPAS. *Journal of the Korean Physical Society*, 67(1):170–174, July 2015. ISSN 0374-4884, 1976-8524. doi: 10.3938/jkps.67.170. URL <http://link.springer.com/10.3938/jkps.67.170>.
- [10] Xiaoning Ding, Wei Liu, Jiajian Shen, Aman Anand, Joshua B. Stoker, Yanle Hu, and Martin Bues. Use of a radial projection to reduce the statistical uncertainty of spot lateral profiles generated by Monte Carlo simulation. *Journal of Applied Clinical Medical Physics*, 18(6):88–96, November 2017. ISSN 15269914. doi: 10.1002/acm2.12184. URL <http://doi.wiley.com/10.1002/acm2.12184>.
- [11] Bruce Faddegon, José Ramos-Méndez, Jan Schuemann, Aimee McNamara, Jungwook Shin, Joseph Perl, and Harald Paganetti. The TOPAS tool for particle simulation, a Monte Carlo simulation tool for physics, biology and clinical research. *Physica Medica*, 72:114–121, April 2020. ISSN 11201797. doi: 10.1016/j.ejmp.2020.03.019. URL <https://linkinghub.elsevier.com/retrieve/pii/S1120179720300715>.
- [12] A. Ferrari, P.R. Sala, A. Fasso, and J. Ranft. FLUKA: A Multi-Particle Transport Code. Technical Report SLAC-R-773, 877507, December 2005. URL <http://www.osti.gov/servlets/purl/877507-sC9S9L/>.
- [13] Matthias Fippel and Martin Soukup. A Monte Carlo dose calculation algorithm for proton therapy. *Medical Physics*, 31(8):2263–2273, July 2004. ISSN 00942405. doi: 10.1118/1.1769631. URL <http://doi.wiley.com/10.1118/1.1769631>.
- [14] F Fracchiolla, S Lorentini, L Widesott, and M Schwarz. Characterization and validation of a Monte Carlo code for independent dose calculation in proton therapy treatments with pencil beam scanning. *Physics in Medicine and Biology*, 60(21):8601–8619, November 2015. ISSN 0031-9155, 1361-6560. doi: 10.1088/0031-9155/60/21/8601. URL <https://iopscience.iop.org/article/10.1088/0031-9155/60/21/8601>.
- [15] Bernard Gottschalk. Passive Beam Spreading in Proton Radiation Therapy, October 2014. URL <http://huhepl.harvard.edu/~gottschalk>.
- [16] L Grevillot, D Bertrand, F Dessy, N Freud, and D Sarrut. A Monte Carlo pencil beam scanning model for proton treatment plan simulation using GATE/GEANT4. *Physics in Medicine and Biology*, 56(16):5203–5219, August 2011. ISSN 0031-9155, 1361-6560. doi: 10.1088/0031-9155/56/16/008. URL <https://iopscience.iop.org/article/10.1088/0031-9155/56/16/008>.
- [17] Particle Therapy Co-Operative Group. Particle Therapy Co-Operative Group. URL www.ptcog.ch.
- [18] S. Helmbrecht, M. Baumann, W. Enghardt, F. Fiedler, M. Krause, and A. Lühr. Design and implementation of a robust and cost-effective double-scattering system at a horizontal proton beamline. *Journal of Instrumentation*, 11(11):T11001–T11001, November 2016. ISSN 1748-0221. doi: 10.1088/1748-0221/11/11/T11001. URL <https://iopscience.iop.org/article/10.1088/1748-0221/11/11/T11001>.
- [19] IBA-Dosimetry. Giraffe detector, . URL <https://www.iba-dosimetry.com/product/giraffe/>.
- [20] IBA-Dosimetry. Lynx pt detector, . URL <https://www.iba-dosimetry.com/product/lynx-pt/>.
- [21] IBA-Dosimetry. MatriXX One/PT, . URL <https://www.iba-dosimetry.com/product/matrixx-one-pt/>.
- [22] Yingcui Jia, Chris Beltran, Daniel J. Indelicato, Stella Flampouri, Zuofeng Li, and Thomas E. Merchant. Proton therapy dose distribution comparison between Monte Carlo and a treatment planning system for pediatric patients with ependymoma: MC vs TPS. *Medical Physics*, 39(8):4742–4747, July 2012. ISSN 00942405. doi: 10.1118/1.4736413. URL <http://doi.wiley.com/10.1118/1.4736413>.
- [23] B. Jones, S.J. McMahon, and K.M. Prise. The Radiobiology of Proton Therapy: Challenges and Opportunities Around Relative Biological Effectiveness. *Clinical Oncology*, 30(5):285–292, May 2018. ISSN 09366555. doi: 10.1016/j.clon.2018.01.010. URL <https://linkinghub.elsevier.com/retrieve/pii/S0936655518300414>.

- [24] Radiology Key. Interaction of Charged Particles with Matter. URL <https://radiologykey.com/interaction-of-charged-particles-with-matter/>.
- [25] Hongdong Liu, Zuofeng Li, Roelf Slopsema, Liu Hong, Xi Pei, and Xie George Xu. TOPAS Monte Carlo simulation for double scattering proton therapy and dosimetric evaluation. *Physica Medica*, 62:53–62, June 2019. ISSN 11201797. doi: 10.1016/j.ejmp.2019.05.001. URL <https://linkinghub.elsevier.com/retrieve/pii/S1120179719301085>.
- [26] TOPAS MC. TOPAS documentation - Miscellaneous. URL <https://topas.readthedocs.io/en/latest/parameters/scoring/misc.html>.
- [27] Gregg Mckinney. *MCNPX User's Manual, Version 2.7.0*. April 2011.
- [28] Timur Mitin and Anthony L. Zietman. Promise and Pitfalls of Heavy-Particle Therapy. *Journal of Clinical Oncology*, 32(26):2855–2863, September 2014. ISSN 0732-183X, 1527-7755. doi: 10.1200/JCO.2014.55.1945. URL <http://ascopubs.org/doi/10.1200/JCO.2014.55.1945>.
- [29] Gert Moliere. Theorie der Streuung schneller geladener Teilchen II Mehrfach-und Vielfachstreuung. *Zeitschrift für Naturforschung A*, 3(2):78–97, February 1948. ISSN 1865-7109, 0932-0784. doi: 10.1515/zna-1948-0203. URL <https://www.degruyter.com/doi/10.1515/zna-1948-0203>.
- [30] Wayne D Newhauser and Rui Zhang. The physics of proton therapy. *Physics in Medicine and Biology*, 60(8):R155–R209, April 2015. ISSN 0031-9155, 1361-6560. doi: 10.1088/0031-9155/60/8/R155. URL <https://iopscience.iop.org/article/10.1088/0031-9155/60/8/R155>.
- [31] World Health Organization. Cancer. URL <https://www.who.int/news-room/fact-sheets/detail/cancer>.
- [32] H. Paganetti, H. Jiang, S.-Y. Lee, and H. M. Kooy. Accurate Monte Carlo simulations for nozzle design, commissioning and quality assurance for a proton radiation therapy facility. *Medical Physics*, 31(7):2107–2118, June 2004. ISSN 00942405. doi: 10.1118/1.1762792. URL <http://doi.wiley.com/10.1118/1.1762792>.
- [33] Harald Paganetti. *Proton Therapy Physics*, volume 20115763 of *Series in Medical Physics and Biomedical Engineering*. CRC Press, December 2011. ISBN 978-1-4398-3644-6 978-1-4398-3645-3. doi: 10.1201/b11448. URL <https://www.taylorfrancis.com/books/9781439836453>.
- [34] Harald Paganetti, Honggu Jiang, Katia Parodi, Roelf Slopsema, and Martijn Engelsman. Clinical implementation of full Monte Carlo dose calculation in proton beam therapy. *Physics in Medicine and Biology*, 53(17):4825–4853, September 2008. ISSN 0031-9155, 1361-6560. doi: 10.1088/0031-9155/53/17/023. URL <https://iopscience.iop.org/article/10.1088/0031-9155/53/17/023>.
- [35] J. Perl, J. Shin, J. Schümann, B. Faddegon, and H. Paganetti. TOPAS: An innovative proton Monte Carlo platform for research and clinical applications: TOPAS: An innovative proton Monte Carlo platform. *Medical Physics*, 39(11):6818–6837, October 2012. ISSN 00942405. doi: 10.1118/1.4758060. URL <http://doi.wiley.com/10.1118/1.4758060>.
- [36] S W Peterson, J Polf, M Bues, G Ciangaru, L Archambault, S Beddar, and A Smith. Experimental validation of a Monte Carlo proton therapy nozzle model incorporating magnetically steered protons. *Physics in Medicine and Biology*, 54(10):3217–3229, May 2009. ISSN 0031-9155, 1361-6560. doi: 10.1088/0031-9155/54/10/017. URL <https://iopscience.iop.org/article/10.1088/0031-9155/54/10/017>.
- [37] Michael Prusator, Salahuddin Ahmad, and Yong Chen. TOPAS Simulation of the Mevion S250 compact proton therapy unit. *Journal of Applied Clinical Medical Physics*, 18(3):88–95, May 2017. ISSN 15269914. doi: 10.1002/acm2.12077. URL <http://doi.wiley.com/10.1002/acm2.12077>.
- [38] Arabinda Kumar Rath and Narayan Sahoo, editors. *Particle Radiotherapy*. Springer India, New Delhi, 2016. ISBN 978-81-322-2621-5 978-81-322-2622-2. doi: 10.1007/978-81-322-2622-2. URL <http://link.springer.com/10.1007/978-81-322-2622-2>.

- [39] F Renner, J Wulff, R-P Kapsch, and K Zink. Uncertainties in Monte Carlo-based absorbed dose calculations for an experimental benchmark. *Physics in Medicine and Biology*, 60(19):7637–7653, October 2015. ISSN 0031-9155, 1361-6560. doi: 10.1088/0031-9155/60/19/7637. URL <https://iopscience.iop.org/article/10.1088/0031-9155/60/19/7637>.
- [40] M Rovituso. *Fragmentation and lateral scattering of 120 and 200 MeV/u 4He ions in water targets*. PhD thesis.
- [41] Dieter Schardt, Thilo Elsässer, and Daniela Schulz-Ertner. Heavy-ion tumor therapy: Physical and radiobiological benefits. *Reviews of Modern Physics*, 82(1):383–425, February 2010. ISSN 0034-6861, 1539-0756. doi: 10.1103/RevModPhys.82.383. URL <https://link.aps.org/doi/10.1103/RevModPhys.82.383>.
- [42] Wook-Geun Shin, Mauro Testa, Hak Soo Kim, Jong Hwi Jeong, Se Byeong Lee, Yeon-Joo Kim, and Chul Hee Min. Independent dose verification system with Monte Carlo simulations using TOPAS for passive scattering proton therapy at the National Cancer Center in Korea. *Physics in Medicine & Biology*, 62(19):7598–7616, September 2017. ISSN 1361-6560. doi: 10.1088/1361-6560/aa8663. URL <https://iopscience.iop.org/article/10.1088/1361-6560/aa8663>.
- [43] Varian Medical Systems. ProBeam proton therapy systems: features and specifications.
- [44] Yoshihisa Takada. Dual-Ring Double Scattering Method for Proton Beam Spreading. *Japanese Journal of Applied Physics*, 33(Part 1, No.1A):353–359, January 1994. ISSN 0021-4922, 1347-4065. doi: 10.1143/JJAP.33.353. URL <https://iopscience.iop.org/article/10.1143/JJAP.33.353>.
- [45] M. Testa, J. Schümann, H.-M. Lu, J. Shin, B. Faddegon, J. Perl, and H. Paganetti. Experimental validation of the TOPAS Monte Carlo system for passive scattering proton therapy: Experimental validation of TOPAS Monte Carlo. *Medical Physics*, 40(12):121719, November 2013. ISSN 00942405. doi: 10.1118/1.4828781. URL <http://doi.wiley.com/10.1118/1.4828781>.
- [46] F Tommasino, M. Rovituso, S. Fabiano, S. Piffer, C. Manea, S. Lorentini, S. Lanzone, Z. Wang, M. Pasini, W.J. Burger, C. La Tessa, E. Scifoni, M. Schwarz, and M. Durante. Proton beam characterization in the experimental room of the Trento Proton Therapy facility. *Nuclear Instruments and Methods in Physics Research Section A: Accelerators, Spectrometers, Detectors and Associated Equipment*, 869:15–20, October 2017. ISSN 01689002. doi: 10.1016/j.nima.2017.06.017. URL <https://linkinghub.elsevier.com/retrieve/pii/S0168900217306654>.
- [47] Francesco Tommasino, Marta Rovituso, Eleonora Bortoli, Chiara La Tessa, Giada Petringa, Stefano Lorentini, Enrico Verroi, Yuri Simeonov, Ulrich Weber, Pablo Cirrone, Marco Schwarz, Marco Durante, and Emanuele Scifoni. A new facility for proton radiobiology at the Trento proton therapy centre: Design and implementation. *Physica Medica*, 58:99–106, February 2019. ISSN 11201797. doi: 10.1016/j.ejmp.2019.02.001. URL <https://linkinghub.elsevier.com/retrieve/pii/S1120179719300213>.
- [48] Joost M. Verburg and Joao Seco. Dosimetric accuracy of proton therapy for chordoma patients with titanium implants: Proton therapy for chordoma patients with implants. *Medical Physics*, 40(7):071727, June 2013. ISSN 00942405. doi: 10.1118/1.4810942. URL <http://doi.wiley.com/10.1118/1.4810942>.
- [49] Joost Mathijs Verburg, Clemens Grassberger, Stephen Dowdell, Jan Schuemann, Joao Seco, and Harald Paganetti. Automated Monte Carlo Simulation of Proton Therapy Treatment Plans. *Technology in Cancer Research & Treatment*, 15(6):NP35–NP46, December 2016. ISSN 1533-0346, 1533-0338. doi: 10.1177/1533034615614139. URL <http://journals.sagepub.com/doi/10.1177/1533034615614139>.
- [50] Uli Weber and Gerhard Kraft. Design and construction of a ripple filter for a smoothed depth dose distribution in conformal particle therapy. *Physics in Medicine and Biology*, 44(11):2765–2775, November 1999. ISSN 0031-9155, 1361-6560. doi: 10.1088/0031-9155/44/11/306. URL <https://iopscience.iop.org/article/10.1088/0031-9155/44/11/306>.
- [51] A. J. Wroe, R. W. Schulte, S. Barnes, G. McAuley, J. D. Slater, and J. M. Slater. Proton beam scattering system optimization for clinical and research applications: Proton beam scattering system optimization. *Medical Physics*, 40(4):041702, March 2013. ISSN 00942405. doi: 10.1118/1.4793262. URL <http://doi.wiley.com/10.1118/1.4793262>.

-
- [52] Jiankui Yuan, Rodney Ellis, and Mitchell Machtay. Technical Note: An approach to building a Monte Carlo simulation model for a double scattering proton beam system. *Medical Physics*, 45(6):2660–2666, June 2018. ISSN 00942405. doi: 10.1002/mp.12895. URL <http://doi.wiley.com/10.1002/mp.12895>.
- [53] Jiankui Yuan, David Mansur, Min Yao, Tithi Biswas, Yiran Zheng, Rick Jesseph, Jian-Yue Jin, and Mitchell Machtay. An Integrated Framework Based on Full Monte Carlo Simulations for Double-Scattering Proton Therapy. *International Journal of Particle Therapy*, 6(2):31–41, September 2019. ISSN 2331-5180. doi: 10.14338/IJPT-19-00063.1. URL <http://theijpt.org/doi/10.14338/IJPT-19-00063.1>.